Journal of Marine Research, 60, 367–404, 2002

Journal of
MARINE RESEARCH

Volume 60, Number 3

Linear planetary wave dynamics in a 2.5-layer ventilated thermocline model

by Atsushi Kubokawa[1] and Maki Nagakura[1,2]

ABSTRACT

Linear planetary wave dynamics in a 2.5-layer ventilated thermocline model is investigated by a local eigenvalue analysis and simple numerical computations. It is known that there are two types of waves in this system; we refer to one of them as the N-mode (Non-Doppler shift mode), which propagates almost westward, and the other as the A-mode (Advection mode), which propagates almost along the second layer basic current. First, we study the local longwave dynamics, assuming that the wavelength is much longer than the deformation radius and shorter than the gyre scale. It is shown that the N-mode and the A-mode cannot neatly be separated in the ventilated zone, and even in the Rhines and Young pool, a compact A-mode disturbance cannot exist by itself. When anomalous Ekman pumping is applied in the ventilated zone, the N-mode is generated in the forcing region, and the A-mode is generated at the wave front of the N-mode. For diabatic forcing, a similar phenomenon occurs. It is also found that the shadow zone is unstable to longwave disturbances. Secondly, the wave behavior in the linear planetary geostrophic model is numerically investigated. The main features can be interpreted by the local wave dynamics, and the disturbances around the maximum amplitudes are dominated by the waves whose wavenumber vectors are perpendicular to the second layer potential vorticity contours. The amplitude changes during the wave propagation are also discussed. Finally, the effects of the finite wavelength are studied. The N-mode is strongly dispersive at the scale of the Rossby deformation radius, while the A-mode is weakly dispersive. It is also shown that the ventilated zone is unstable to shortwave disturbances, although it is stable to longwave disturbances.

1. Graduate School of Environmental Earth Science, Hokkaido University, Sapporo 060-0810, Japan. ***email: kubok@ees.hokudai.ac.jp***

2. Present address: Advanced Simulation Technology of Mechanics R&D Co. Ltd., Riken, 2-1 Hirosawa, Wako 351-0198, Japan.

1. Introduction

Our understanding of the oceanic thermocline structure has made great progress during recent decades since the advent of the ventilated thermocline theory (Luyten *et al.,* 1983) and the potential vorticity homogenization theory (Rhines and Young, 1982; Young and Rhines, 1982). According to these theories, the potential vorticity distribution in the thermocline is distorted very much from zonal uniformity because of the Lagrangian conservative nature of the potential vorticity. This distorted potential vorticity distribution and advection make the planetary wave dynamics very different from that in a resting ocean.

Dynamics of the planetary waves in the oceanic gyre have recently been investigated extensively. Those studies seem to be motivated by recent observations. Chelton and Schlax (1996) and Polito and Cornillon (1997) showed from satellite observations of the sea surface height (SSH) anomaly that the first baroclinic Rossby wave propagates at a phase speed higher than that expected from the local stratification. On this problem, Killworth *et al.* (1997) showed that the longwave phase speed of the gravest baroclinic mode in an oceanic gyre (baroclinic shear flow) is enhanced, and the estimated phase speeds agree well with observed ones in almost all regions. Liu (1999a) and deSzoeke and Chelton (1999) discussed the enhancement of the phase speed analytically, showing that the uniformity of subsurface potential vorticity is crucial for this enhancement of the wave speed.

The effects of the vertical structure of the oceanic gyre on higher baroclinic modes are much more significant than that on the gravest mode because their phase speeds are comparable with, or smaller than, the advection velocity. Using a 2.5-layer quasi-geostrophic model, Liu (1999a,b) showed that the second mode tends to propagate along the mean current in the second layer, and argued that this nature explains the southward spreading of the subsurface temperature anomaly associated with the interdecadal variability of the sea surface temperature reported by, for example, Deser *et al.* (1996) and by Yasuda and Hanawa (1997). Liu (1999b) carried out several numerical experiments, to show that similar thermocline responses to those expected from the linear theory occur in the numerical models.

Very recently, Dewar and Huang (2001) and Stephens *et al.* (2001) treated similar problems. Dewar and Huang discussed the wave dynamics in a multi-layer quasi-geostrophic model based on the characteristic theory. On the other hand, Stephans *et al.* solved a 2-layer planetary geostrophic model and discussed the wave property of the second mode. Both papers compared the analytical results with more sophisticated numerical models.

Although the above works have outlined the wave dynamics and their gyre-scale propagations very well, it seems to the authors that some uncertainties still remain. For example, the full dispersion relation of waves and its relation to wave propagation in the oceanic gyre have not been reported. In the present paper, adopting a 2.5-layer version of the LPS model (Luyten *et al.,* 1983) as the basic state, we attempt to clarify the linear wave dynamics in the thermocline, focusing on (1) local longwave properties and their relation to

wave propagation in the oceanic gyre, (2) stability, (3) adjustment process of the thermocline to anomalous atmospheric forcing, and (4) dependence on the wavelength.

In a system in which the direction of the potential vorticity gradient depends on depth as in the ventilated thermocline, the vertical structure and the group velocity of a longwave disturbance depend on the direction of the wavenumber vector in general. Combination of the local eigenvalue analysis and simple numerical computation of the temporal evolution will help us to image the wave behavior in such a system. The stability of the ventilated thermocline should also be addressed, because the potential vorticity distribution in the ventilated thermocline satisfies a necessary condition for baroclinic instability (see, e.g., Chapter 7.13 in Pedlosky, 1987). The adjustment process of the ventilated thermocline is an important problem to understand ocean climate variability. This process must be related to the dispersive nature, as well. Steady responses of the LPS model to atmospheric anomalous forcing have been studied by Huang and Pedlosky (1999). In the present work, temporal evolution of the linear disturbance after the forcing is turned on will be discussed. The relative vorticity term, which has been neglected in the gyre scale dynamics, may also be important to stability and wave propagation. Although the 2.5-layer ventilated thermocline model may be too simple to be directly applied to the real ocean, it is meaningful to investigate the wave dynamics in detail, since the model can be regarded as one of the standard models widely used to discuss basic ocean dynamics.

After formulating the problem in Section 2, the local dynamics of linear longwaves are investigated mainly by eigenvalue analysis in Section 3. In this section, the stability of the ventilated thermocline to a longwave disturbance is also examined, and several numerical examples of free wave propagation and forced wave responses are presented. Section 4 discusses the gyre-scale propagation referring to results obtained by local eigenvalue analysis. In Section 5, we briefly discuss the dependence of local eigenvalue solutions on the wavelength including the relative vorticity term. The results are summarized in Section 6.

2. Formulation of the problem

A 2.5-layer planetary geostrophic model is used in the main part of the present study. The set of model equations is

$$-fv_j = -\frac{1}{a\cos\theta}\frac{\partial p_j}{\partial\lambda}, \quad fu_j = -\frac{1}{a}\frac{\partial p_j}{\partial\theta} \tag{2.1}$$

$$\frac{\partial h_j}{\partial t} + \frac{1}{a\cos\theta}\left\{\frac{\partial}{\partial\lambda}h_j u_j + \frac{\partial}{\partial\theta}h_j v_j\cos\theta\right\} = -(2-j)w_e - (-1)^j w_d \tag{2.2}$$

$$p_2 = \gamma_2(h_1 + h_2), \quad p_1 = p_2 + \gamma_1 h_1 \tag{2.3}$$

where the subscript j ($=1, 2$) denotes the layer number, a is the radius of the earth, λ and θ are the longitude and latitude respectively, u_j and v_j are the eastward and northward components of the velocity, h_j is the layer thickness, f is the Coriolis parameter, γ_j is the

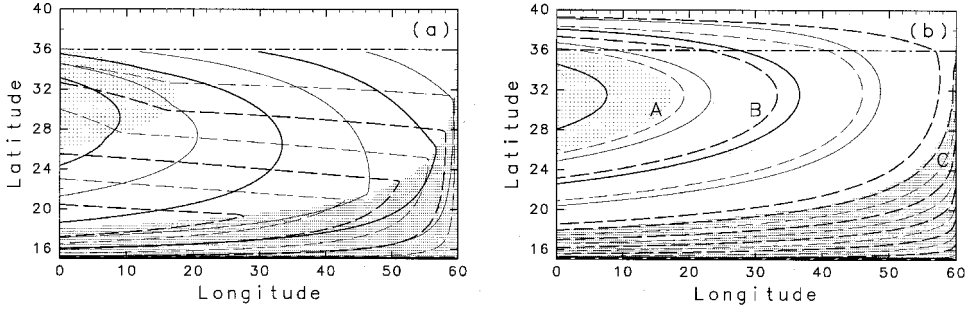

Figure 1. The solution of the ventilated thermocline model used as the basic state of the present study: (a) upper layer, and (b) second layer. Solid lines denote the pressure (contour interval is 0.5×10^3 Kg m^{-1} s^{-2}) and dashed lines denote the potential thickness (contour interval is 7.5×10^3 m s). Heavy shade denotes the shadow zone where the second layer is at rest, and light shade denotes the RY pool where the second layer potential vorticity is homogenized. The letters A, B and C denote locations where local eigenvalues are calculated.

reduced gravity ($=g(\rho_{j+1} - \rho_j)/\rho_0$), w_e is the Ekman pumping velocity, and w_d is a diabatic forcing, which is thought to represent surface cooling ($w_d > 0$) or warming ($w_d < 0$).

Since we study the wave dynamics in the oceanic gyre, we divide the variables into two parts, the basic state and wave field;

$$u_j = U_j(\lambda, \theta) + u'_j(\lambda, \theta, t), \quad v_j = V_j(\lambda, \theta) + v'_j(\lambda, \theta, t), \quad p_j = P_j(\lambda, \theta) + p'_j(\lambda, \theta, t)$$
$$h_1 = H_1(\lambda, \theta) + \eta_1(\lambda, \theta, t), \quad h_2 = H_2(\lambda, \theta) + \eta_2(\lambda, \theta, t) - \eta_1(\lambda, \theta, t)$$
$$w_e = W_e(\theta) + w'_e(\lambda, \theta, t), \quad w_d = w'_d(\lambda, \theta, t)$$

where U_j, V_j, P_j and H_j represent the basic state which is forced by the Ekman pumping W_e. We assume that the second layer outcrops at $f = f_1$, where f_1 is a constant. In this case, the solution for the basic state is the 2.5-layer version of the LPS model, and the explicit form of the solution is shown in Appendix A. The model domain and parameters used in this study are as follows: The latitude of the northern boundary of the subtropical gyre, θ_N, is 40N, that of the southern boundary, θ_S, is 15N, the outcrop latitude, θ_1, is 36N, and the longitudinal extent of the ocean, λ_e, is 60°. The reduced gravities are $\gamma_1 = \gamma_2 = 0.8 \times 10^{-2}$ m/s^2, and the thermocline depth at the eastern boundary, $H_0 = H_2(\lambda_e, \theta)$, is 500 m. The Ekman pumping, W_e, is assumed to be

$$W_e = -10^{-6} \sin \frac{\pi(\theta - \theta_N)}{\theta_S - \theta_N} \text{[m/s]}.$$

Figure 1 depicts the pressure, P_j, and the potential thickness, H_j/f, (reciprocal of the potential vorticity) for both layers of the basic state (the solution of the LPS model). The domain is divided into three zones: the eastern shadow zone (dark shade in Fig. 1), the ventilated zone and the western pool zone (light shade). In the western pool zone, the

potential vorticity in the second layer is assumed to be homogenized; this region is referred to as the Rhines and Young pool (RY pool) hereafter. The waves have different natures in the different zones.

The equation for the linear wave field can be written in terms of η_1 and η_2 after some manipulation as

$$\frac{\partial}{\partial t}\begin{pmatrix}\eta_1\\ \eta_2\end{pmatrix}+\frac{1}{a\cos\theta}\mathsf{A}\frac{\partial}{\partial\lambda}\begin{pmatrix}\eta_1\\ \eta_2\end{pmatrix}+\frac{1}{a}\mathsf{B}\frac{\partial}{\partial\theta}\begin{pmatrix}\eta_1\\ \eta_2\end{pmatrix}+\mathsf{C}\begin{pmatrix}\eta_1\\ \eta_2\end{pmatrix}=\mathbf{W} \tag{2.4}$$

where A, B and C are 2×2 matrices and $\mathbf{W}$ is a vector:

$$\mathsf{A}=\begin{pmatrix}U_2-\dfrac{\beta}{f^2}\gamma_1H_1 & \gamma_2\left(\dfrac{H_1}{f}\right)_y\\ -\dfrac{\beta}{f^2}\gamma_1H_1 & -\dfrac{\beta}{f^2}\gamma_2H\end{pmatrix},\quad \mathsf{B}=\begin{pmatrix}V_2 & -\dfrac{\gamma_2}{f}H_{1x}\\ 0 & 0\end{pmatrix}, \tag{2.5}$$

$$\mathsf{C}=\begin{pmatrix}-\dfrac{\beta}{f}V_1 & 0\\ -\dfrac{\beta}{f^2}\gamma_1H_{1x} & -\dfrac{\beta}{f^2}\gamma_2H_x\end{pmatrix},\quad \mathbf{W}=\begin{pmatrix}-w_e+w_d\\ -w_e\end{pmatrix}. \tag{2.6}$$

Here, $\beta=a^{-1}df/d\theta$ and subscripts, x and y, denote the zonal derivative and meridional derivative, e.g.,

$$H_{1x}=\frac{1}{a\cos\theta}\frac{\partial H_1}{\partial\lambda},\quad H_{1y}=\frac{1}{a}\frac{\partial H_1}{\partial\theta}.$$

The quantity H_j/f is referred to as the potential thickness in this paper and is used instead of the potential vorticity f/H_j, since H_j/f is somewhat more convenient than the potential vorticity in the formulation of the present planetary geostrophic model.

The existence of terms proportional to η_1 and η_2 in (2.4) means that disturbances in η_1 and η_2 do not simply propagate as waves but can change locally even when the initial values of η_1 and η_2 are spatially constant and $\mathbf{W}=0$. If we change the dependent variables by using a matrix G as,

$$\begin{pmatrix}\zeta_1\\ \zeta_2\end{pmatrix}=\mathsf{G}^{-1}\begin{pmatrix}\eta_1\\ \eta_2\end{pmatrix}, \tag{2.7}$$

and G satisfies

$$\mathsf{G}^{-1}\left(\frac{1}{a\cos\theta}\mathsf{A}\frac{\partial\mathsf{G}}{\partial\lambda}+\frac{1}{a}\mathsf{B}\frac{\partial\mathsf{G}}{\partial\theta}+\mathsf{C}\mathsf{G}\right)=0, \tag{2.8}$$

we can eliminate the term proportional to the wave amplitude, and (2.4) can be rewritten as

$$\frac{\partial}{\partial t}\begin{pmatrix}\zeta_1\\ \zeta_2\end{pmatrix}+\frac{1}{a\cos\theta}\mathsf{A}'\frac{\partial}{\partial\lambda}\begin{pmatrix}\zeta_1\\ \zeta_2\end{pmatrix}+\frac{1}{a}\mathsf{B}'\frac{\partial}{\partial\theta}\begin{pmatrix}\zeta_1\\ \zeta_2\end{pmatrix}=\mathbf{W}', \tag{2.9}$$

where

$$\mathsf{A}' = \mathsf{G}^{-1}\mathsf{A}\mathsf{G}, \quad \mathsf{B}' = \mathsf{G}^{-1}\mathsf{B}\mathsf{G}, \quad \mathbf{W}' = \mathsf{G}^{-1}\mathbf{W}$$

In this case, constant ζ_1 and ζ_2 give a steady solution if $\mathbf{W} = 0$. The matrix G satisfying (2.8) in each zone can be found as,

for the Rhines and Young pool, $$\mathsf{G} = \begin{pmatrix} \frac{\gamma_2 f}{P_1} & 0 \\ \frac{\gamma_2 f}{P_1} & \frac{f}{H} \end{pmatrix},$$

for the ventilated zone, $$\mathsf{G} = \begin{pmatrix} \frac{f}{H} & 0 \\ 0 & \frac{f}{H_1} \end{pmatrix},$$

and for the shadow zone $$\mathsf{G} = \begin{pmatrix} \frac{f_1}{H_1} & 0 \\ 0 & \frac{f_1}{H_0} \end{pmatrix}.$$

3. Local dynamics

a. Outline of the eigenvalue problem

In this section we assume that the horizontal scale of the disturbance is much smaller than the gyre scale. Under this assumption, A and B in (2.4) become constant matrices and C vanishes. The resulting equation is the same as that obtained under the quasi-geostrophic (QG) approximation neglecting relative vorticity. The solution of the full equation (2.4) will be discussed in Section 4, and the effect of the relative vorticity under the QG approximation will be addressed in Section 5.

Introducing the local Cartesian coordinates whose origin is at (λ_0, θ_0), we obtain

$$\frac{\partial}{\partial t}\begin{pmatrix} \eta_1 \\ \eta_2 \end{pmatrix} + \mathsf{A}\frac{\partial}{\partial x}\begin{pmatrix} \eta_1 \\ \eta_2 \end{pmatrix} + \mathsf{B}\frac{\partial}{\partial y}\begin{pmatrix} \eta_1 \\ \eta_2 \end{pmatrix} = \mathbf{W}, \tag{3.1}$$

where

$$x = a\cos\theta_0(\lambda - \lambda_0), \quad y = a(\theta - \theta_0).$$

Since this equation does not depend on the horizontal scale, the dispersive nature of waves comes only from the direction of the wavenumber vector. If we consider a disturbance whose amplitude varies only in one direction, (3.1) becomes

$$\frac{\partial}{\partial t}\begin{pmatrix} \eta_1 \\ \eta_2 \end{pmatrix} + \mathsf{D}\frac{\partial}{\partial s}\begin{pmatrix} \eta_1 \\ \eta_2 \end{pmatrix} = \mathbf{W}, \tag{3.2}$$

where s is the distance in the direction of the wave propagation. If we write this direction in terms of the angle φ measured from the east in the counterclockwise direction, the variable s becomes

$$s = \frac{x}{\cos\varphi} = \frac{y}{\sin\varphi}$$

and

$$\mathsf{D} = \mathsf{A}\cos\varphi + \mathsf{B}\sin\varphi.$$

The eigenvalue of the matrix D gives the phase speed in the direction of φ, and the eigenvector gives the vertical structure of the wave. The eigenvalues of the matrix D are the same as those of $\mathsf{D}' = \mathsf{A}'\cos\varphi + \mathsf{B}'\sin\varphi$ in (2.9).

The eigenvalues of the matrix D can be written as

$$c_{\pm} = \frac{1}{2}\{(d_{11} + d_{22}) \pm \sqrt{(d_{11} - d_{22})^2 + 4d_{12}d_{21}}\}, \tag{3.3}$$

where d_{ij} is the ij-component of D. The explicit form of the eigenvalue is shown in Appendix B. The double sign in (3.3) denotes that there are two vertical modes. Since $d_{11} + d_{22} \propto \sin(\varphi + \varphi_0)$ where φ_0 is a constant and $\sqrt{(d_{11} - d_{22})^2 + 4d_{12}d_{21}}$ is a periodic function of φ with period π, we can easily demonstrate that

$$c_{\pm}(\varphi) = -c_{\mp}(\varphi + \pi) = -c_{\mp}(\varphi - \pi). \tag{3.4}$$

Therefore, one of $c_+(\varphi)$ or $c_-(\varphi)$ for $0 \le \varphi < 2\pi$ gives the complete set of eigenvalues.

When $(d_{11} - d_{22})^2 + 4d_{12}d_{21} < 0$, the eigenvalue has an imaginary part, that is, the ventilated thermocline is unstable. After some manipulation, $(d_{11} - d_{22})^2 + 4d_{12}d_{21}$ can be written as

$$\left[-\frac{\beta\gamma_1}{f^2} H_1 \cos\varphi + \gamma_2 \hat{\mathbf{z}} \cdot (\mathbf{K} \times \nabla((H_1 - H_2)/f)) \right]^2 + 4\gamma_2^2 (\mathbf{K} \times \nabla(H_1/f)) \cdot (\mathbf{K} \times \nabla(H_2/f)), \tag{3.5}$$

where $\mathbf{K} = (\cos\varphi, \sin\varphi)$ and $\hat{\mathbf{z}}$ is the unit vector positive upward. This equation means that the second term of (3.5) must be negative and the first term must be small for c to have an imaginary part. The first condition is the well known necessary condition for baroclinic instability, that is, for baroclinic instability to occur, the potential vorticity gradient, $\nabla(f/H_j)$, along the perturbation trajectory must be positive in one layer and negative in the other (see, e.g., Pedlosky, 1987). The second condition is that the phase speeds of the two modes are close to each other (see, e.g., Craik, 1985).

The group velocity, $\mathbf{c}_g = (c_{gx}, c_{gy})$, is obtained by

$$c_{gx} = \frac{\partial c}{\partial(\cos\varphi)}, \quad c_{gy} = \frac{\partial c}{\partial(\sin\varphi)}. \tag{3.6}$$

If $c(\varphi)$ has the form

$$c(\varphi) = a\cos\varphi + b\sin\varphi, \tag{3.7}$$

the wave is nondispersive, and the curve given by the terminal point of the phase velocity vector, $c(\varphi)\mathbf{K} = (c(\varphi)\cos\varphi, c(\varphi)\sin\varphi)$, becomes a circle, i.e.,

$$\left(c(\varphi)\cos\varphi - \frac{a}{2}\right)^2 + \left(c(\varphi)\sin\varphi - \frac{b}{2}\right)^2 = \frac{1}{4}(a^2 + b^2). \tag{3.8}$$

In this case, the group velocity does not depend on the direction and is the same as the maximum phase velocity. This type of solution can be obtained in the RY pool where the potential vorticity in the second layer is assumed to be homogenized (see next subsection). In general, the solution has a more complex form. However, it can easily be shown that the group velocity of the wave having the maximum phase speed coincides with its phase velocity if c is real. To show this, let us introduce new Cartesian coordinates (x', y'), where the x' axis is taken in the direction of the wavenumber vector of the maximum phase speed. Writing the wavenumber vector in this coordinate system as (k, l), the group velocity can be written as

$$c_{gx'} = \left.\frac{\partial kc}{\partial k}\right|_{l=0}, \quad c_{gy'} = \left.\frac{\partial kc}{\partial l}\right|_{l=0}. \tag{3.9}$$

Since c does not depend on k and $(\partial/\partial l)c$ must vanish at $l = 0$, we obtain

$$c_{gx'} = c, \quad c_{gy'} = 0, \tag{3.10}$$

for the wave with the maximum phase velocity. For the steady solution whose c is zero, taking the x' axis in the direction of the wavenumber vector of the stationary wave, we find that the group velocity is perpendicular to the wavenumber vector, because $c = 0$ but $(\partial/\partial l)c|_{l=0} \neq 0$ in this case. To give a more detailed discussion, we need to consider the explicit form of the matrix D.

b. P.V. homogenized pool

In the Rhines and Young pool, the solution is very simple, because the potential vorticity in the second layer is uniform. Since the second term in the square root in (B.2) or that in (3.5) vanishes, the eigenvalue c can be written as

$$c = \frac{1}{2}\left\{-\frac{\beta}{f^2}P_1\cos\varphi + \mathbf{U}_2\cdot\mathbf{K} + \left|\frac{\beta}{f^2}P_1\cos\varphi + \mathbf{U}_2\cdot\mathbf{K}\right|\right\}, \tag{3.11}$$

where we have taken only the solution with a plus sign in (3.3) since $c_-(\varphi) = c_+(\varphi + \pi)$ as mentioned in the preceding subsection. This equation means that the eigenvalue can be divided into

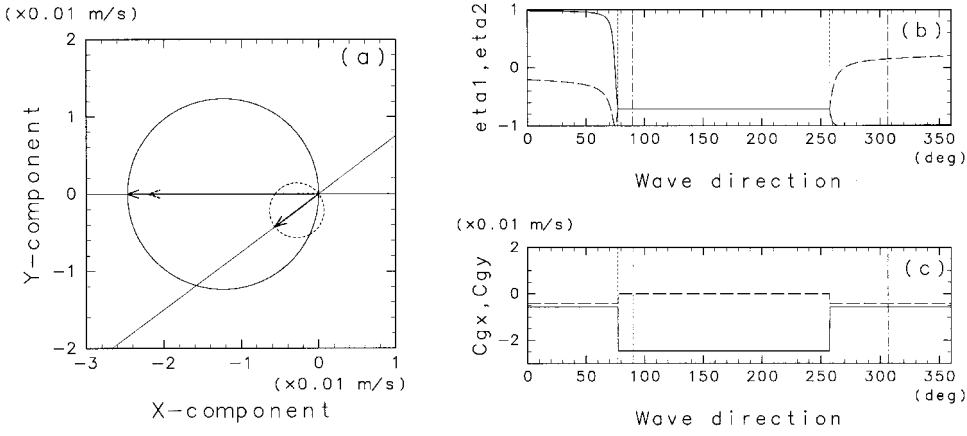

Figure 2. Eigenvalue solution in the RY pool (location A in Fig. 1: longitude = 15°, latitude = 30°) as a function of the direction of wavenumber vector: (a) two-dimensional diagram of the phase velocity vector, ($c(\varphi)\cos\varphi$, $c(\varphi)\sin\varphi$), (b) eigenvectors (vertical structure) and (c) group velocities. In panel (a), the solid curve corresponds to the *N*-mode, the dashed curve to the *A*-mode. The westward longer arrow (solid) is the maximum phase velocity vector of the *N*-mode which is identical to the group velocity; the westward shorter arrow (dotted) is the group velocity without the basic flow. The southwestward arrow denotes the basic current velocity in the second layer. In panel (b), the solid line and the dashed line denote η_1 and η_2, respectively, and their amplitudes are normalized as satisfying $\sqrt{\eta_1^2 + \eta_2^2} = 1$. In panel (c), the solid line and the dashed lines denote c_{gx} and c_{gy}, respectively. The vertical dotted lines and dash-dotted lines in panel (b) and (c) denote the wave directions where the *N*-mode and the *A*-mode are separated, and those where the solutions are stationary ($c = 0$), respectively.

$$c = \begin{cases} -\dfrac{\beta}{f^2} P_1 \cos\varphi & \text{for } \dfrac{\beta}{f^2} P_1 \cos\varphi + \mathbf{U}_2 \cdot \mathbf{K} \le 0 \\ \mathbf{U}_2 \cdot \mathbf{K} & \text{for } \dfrac{\beta}{f^2} P_1 \cos\varphi + \mathbf{U}_2 \cdot \mathbf{K} > 0 \ . \end{cases} \tag{3.12}$$

As noted in the preceding section, the curves consisting of the terminal points of the phase velocity vectors, $c\mathbf{K} = (c(\varphi)\cos\varphi, c(\varphi)\sin\varphi)$, are circles (see Fig. 2a). The group velocity of each mode becomes a constant vector:

$$\mathbf{c}_g = \begin{cases} \left(-\dfrac{\beta}{f^2} P_1, 0 \right) & \text{for } \dfrac{\beta}{f^2} P_1 \cos\varphi + \mathbf{U}_2 \cdot \mathbf{K} \le 0 \\ \mathbf{U}_2 & \text{for } \dfrac{\beta}{f^2} P_1 \cos\varphi + \mathbf{U}_2 \cdot \mathbf{K} > 0 \ . \end{cases} \tag{3.13}$$

Therefore, the former mode propagates westward independent of the mean flow direction, which is always higher than the first mode phase speed in the resting ocean with the same density structure:

$$c_1 = -\frac{1}{2}\beta f^{-2}\{P_1 + (P_1^2 - 4\gamma_1\gamma_2 H_1 H_2)^{1/2}\}, \tag{3.14}$$

(see also deSzoeke and Chelton, 1999), and the latter mode is purely advective by the second layer mean flow (see also Fig. 2c). After Liu (1999b), we refer to these waves as the *N*-mode (non-Doppler-shift mode) and the *A*-mode (advection mode), respectively, and we represent these modes by subscripts, *N* and *A*, hereafter. The angles of the wavenumber vector, φ, dividing the two modes are given by

$$\varphi = \tan^{-1}\left[\frac{\partial P_2/\partial y - \beta P_1/f}{\partial P_2/\partial x}\right] \tag{3.15}$$

and the angles at location A in Figure 1 (30° longitude, 15° latitude) are 78 degrees and 258 degrees (see Fig. 2c).

The corresponding eigenvectors, $\mathbf{R}_N$ and $\mathbf{R}_A$, which represent the relation between η_1 and η_2, are given by

$$\mathbf{R}_N = \begin{pmatrix} 1 \\ 1 \end{pmatrix}, \quad \mathbf{R}_A = \begin{pmatrix} \hat{\mathbf{z}} \cdot (\mathbf{K} \times \nabla(H_1/f)) \\ \dfrac{\beta}{f^2}\gamma_1 H_1 \cos^2\varphi \end{pmatrix}. \tag{3.16}$$

Figure 2b shows $\mathbf{R}(\varphi)$. Since $\eta_2 - \eta_1$ is zero, the *N*-mode has no potential vorticity anomaly in the second layer. On the other hand, the *A*-mode appears mainly in η_1 and is characterized by the second layer potential vorticity anomaly. The fact that the potential vorticity in the second-layer in the basic state is homogeneous in the RY pool gives the reason why the propagation speed of the *A*-mode coincides with the second layer advection velocity. Although the group velocities of both modes are independent of the wavenumber vector, the vertical structure of the *A*-mode depends on it. In Figure 2b, we can see that η_j $(\varphi = 0) = -\eta_j$ $(\varphi = 2\pi)$. This means that the *A*-mode cannot have a closed contour by itself.

The wavenumber vector directions giving stationary solutions are meridional for the *N*-mode, and are perpendicular to the basic flow in the second layer for the *A*-mode. The vertical dash-dotted lines in Figure 2b and c denote these angles. The directions of the group velocities are perpendicular to these wavenumber vectors as mentioned in the preceding subsection.

Figure 3 shows the temporal evolution of an initial Gaussian-shape disturbance given only in η_1. The temporal evolution is obtained by numerical computation of (3.1). The variables are nondimensionalized by the horizontal scale *L*, the initial amplitude in η_1 and the time scale $L/|c_1|$, where c_1 is given by (3.14). The initial axisymmetric disturbance separates into the *N*-mode and *A*-mode; the *N*-mode propagates westward at the speed $\beta P_1/f^2$, and the *A*-mode propagates at the speed $\mathbf{U}_2$. However, this separation is not complete, and a thin bridge connecting these disturbances remains. Since the potential thickness anomaly, $(\eta_2 - \eta_1)/f$, in the second layer is just advected by $\mathbf{U}_2$, we can see that

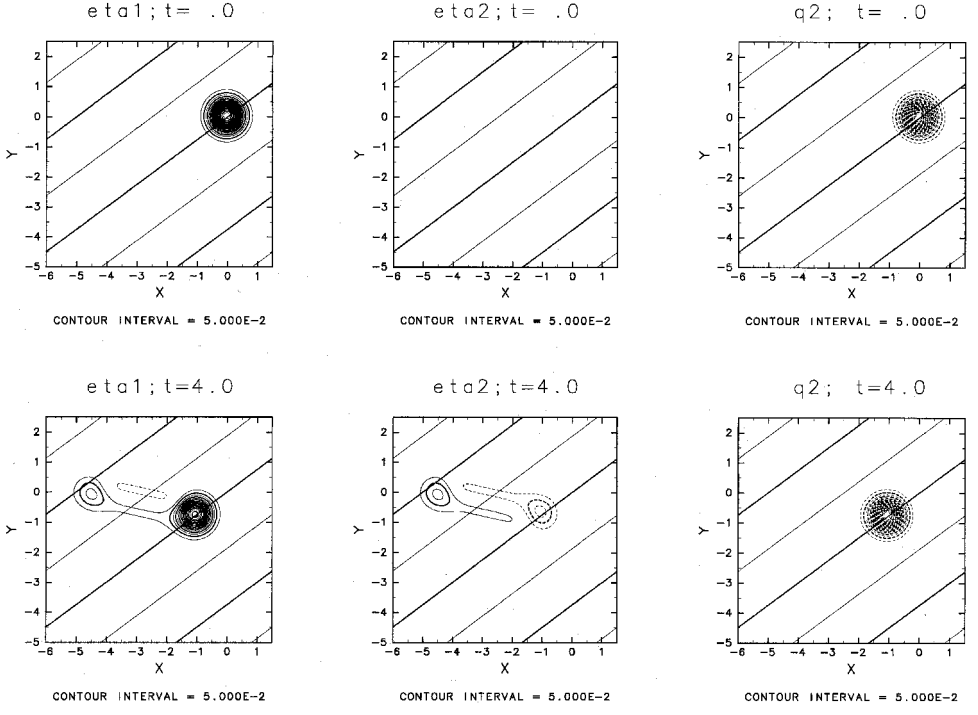

Figure 3. Temporal evolution of an initial disturbance in the RY pool at location A in Figure 1: η_1 (left column), η_2 (middle column) and $\eta_2 - \eta_1$ (right column). The initial disturbance is given by $\eta_1 = \exp\{(x^2 + y^2)/(2L)^2\}$, $\eta_2 = 0$, and the horizontal coordinates are normalized by L and time by $L/|c_1|$ where L is an arbitrary length scale and c_1 is given by (3.14). The contour intervals are denoted below each panel. The slanted straight lines are the stream lines of the second-layer basic flow.

this bridge consists of the *N*-mode. This means that the *A*-mode or the second layer potential thickness anomaly always generates the *N*-mode as the *A*-mode propagates. This corresponds to the fact that the *A*-mode does not have a closed contour of η_j by itself. If the initial disturbance has no potential vorticity anomaly in the second layer, i.e., $\eta_1 = \eta_2$, the disturbance propagates as *N*-mode keeping the axisymmetric shape and there is no *A*-mode wave generation.

c. Ventilated zone

i. Free wave propagation. The eigenvalue, $c(\varphi)$, the eigenvector, (η_1, η_2), and the group velocity, $\mathbf{c}_g(\varphi)$, at location B in Figure 1 are shown in Figure 4. In the present case, the waves cannot be strictly separated into the two modes. We refer, however, to the wave mode with $c_{gx} \leq \bar{c}_{gx}$ as *the N-mode* and the wave mode with $c_{gx} > \bar{c}_{gx}$ as *the A-mode* just for convenience, where $\bar{c}_{gx}$ is the zonal component of the averaged group velocity, $\bar{c}_{gx} =$

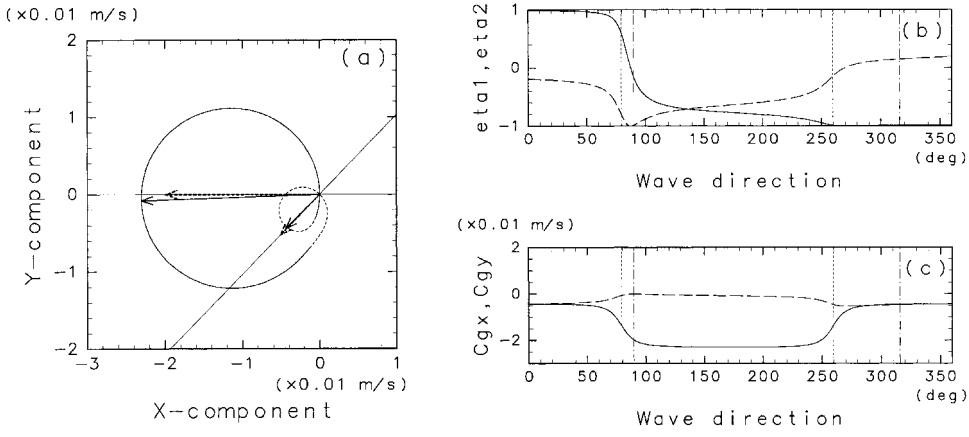

Figure 4. Same as Figure 2 but for the ventilated zone (location B in Figure 1: longitude = 30°, latitude = 30°). In panel (a), the westward and southwestward solid arrows denote the typical group velocity vectors of the *N*-mode and the *A*-mode, respectively, and the southwestward dotted arrow denotes the basic flow velocity in the second layer.

$\int_0^{2\pi} c_{gx}(\varphi)d\varphi$. The directions, φ, separating these modes are denoted by the vertical dotted lines in Figs. 4b and c.

The wavenumber vector of the *N*-mode stationary wave ($c = 0$) is directed meridionally and that of the *A*-mode is perpendicular to the second layer basic current. This is demonstrated in Appendix B. The maximum phase speeds, however, are not perpendicular to these wavenumber vectors; the direction of the maximum phase speed of the *N*-mode is sifted slightly leftward from the west, and that of the *A*-mode slightly rightward from the second layer current velocity (Appendix B). The westward phase speed of the *N*-mode is always higher than that in the resting ocean with the same density stratification, while the *A*-mode phase speed along the basic current is always smaller than the second layer current velocity. These differences from the waves in the P.V. homogenized pool are caused by the potential vorticity distribution in the second layer; the second layer P.V. distribution tends to force the *A*-mode to propagate upstream relative to the basic current, and the southward advection of second layer potential vorticity anomaly affects the *N*-mode propagation.

Since the wave properties depend on the wave direction, it is not easy to compare the numerical results to the eigenvalue solutions. So, we define a typical *N*-mode and *A*-mode using the central direction of each mode, i.e.,

$$\varphi = \frac{\varphi_{AN} + \varphi_{NA}}{2} \quad \text{for typical } N\text{-node}$$

$$\varphi = \frac{\varphi_{AN} + \varphi_{NA}}{2} + \pi \quad \text{for typical } A\text{-node}$$

where φ_{AN} and φ_{NA} are the wave directions separating the two modes (denoted by the vertical dotted lines in Figs. 4b and c). The group velocities of these typical modes are

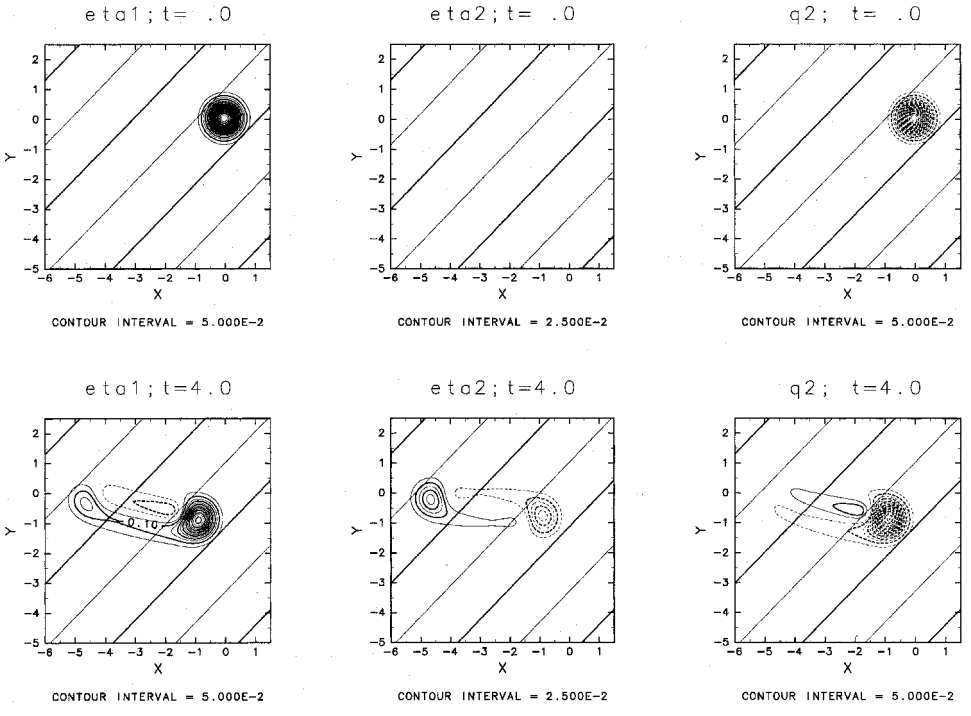

Figure 5. Same as Figure 3 but for the ventilated zone (location B in Fig. 1).

shown by arrows in Figure 4a. The gyre-scale distributions of the group velocities and vertical structures of the typical modes will be discussed in Section 4.

The temporal evolutions of initial axisymmetric disturbances are shown in Figures 5 and 6. In these figures, the variables are nondimensionalized by L and c_1 as in Figure 3. When the initial disturbance is given only in η_1 (Fig. 5), the solution is similar to that shown in Figure 3, in which the disturbance separates into two modes. The second layer thickness anomaly, $(\eta_2 - \eta_1)$, however, disperses as well. The propagation velocities of the maximum η_1 and of the maximum η_2 agree well with the typical A-mode group velocity and the typical N-mode group velocity defined above, respectively; the locations of the maximum η_1 and maximum η_2 at $t = 4$ are $(-0.90, -0.91)$ and $(-4.65, -0.2)$, and those calculated from the typical group velocities are $(-0.88, -0.89)$ and $(-4.62, -0.17)$. The vertical structures, η_2/η_1, at these locations also coincide with the typical ones; those values at the locations of the maximum η_1 and maximum η_2 at $t = 4$ are -0.18 and 0.84, and those of the typical modes are -0.18 and 0.84.

The N-mode wave front does not appear in the second layer thickness anomaly, $\eta_2 - \eta_1$, because $\eta_2/\eta_1 \simeq 1$ there, and only the A-mode and the bridge connecting the A-mode peak and the N-mode peak can be seen. The bridge part is barotropic (i.e., $\eta_1\eta_2 > 0$) and $\eta_2(\eta_2 - \eta_1)$ is negative, suggesting that this part consists mainly of waves around $\varphi \simeq$ 240–270 degrees in Figure 4b.

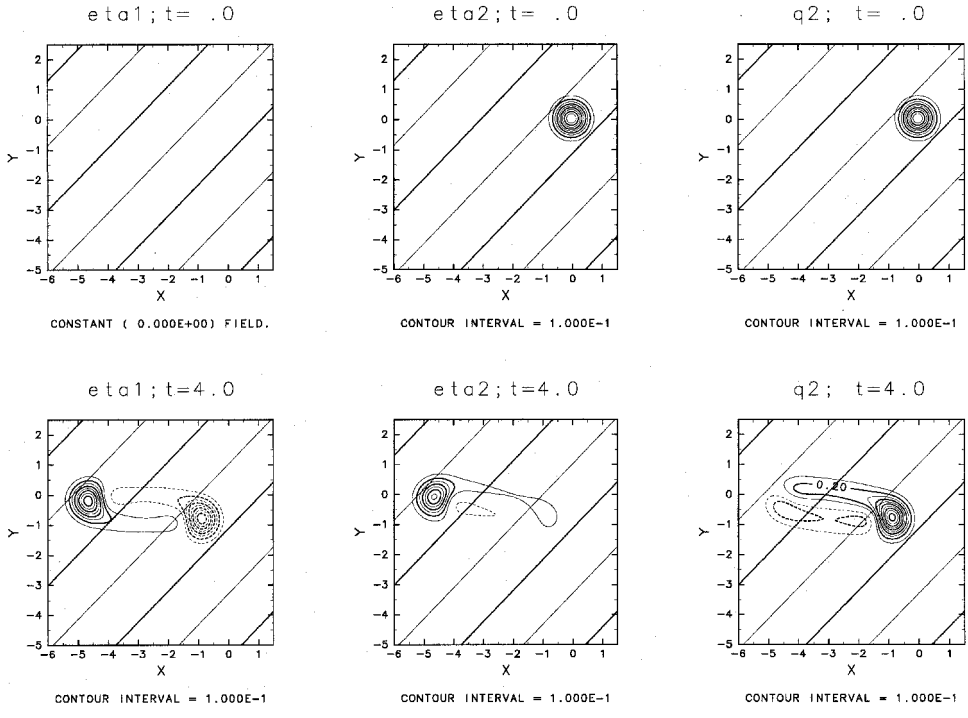

Figure 6. Same as Figure 5 but for the initial disturbance given only in η_2.

Figure 6 depicts the evolution when the initial disturbance is given only in η_2. The initial disturbance separates into two modes, and the part of the bridge connecting the two mode centers has baroclinic structure (i.e., $\eta_1\eta_2 < 0$) with positive $\eta_2(\eta_2 - \eta_1)$, which suggests that this part consists mainly of waves around $\varphi \simeq 60$–90 degrees in Figure 4b. From these figures, we speculate that this part is barotropic when the *A*-mode disturbance is dominant but baroclinic when the *N*-mode disturbance is dominant. The bridge always has a barotropic structure in the RY pool, because the potential thickness anomaly does not disperse in that region. Temporal evolution of the axisymmetric initial disturbance with arbitrary vertical structure can be constructed from these two cases.

ii. Stability. The waves described in the preceding subsection were stable, but this does not necessarily mean that the ventilated zone is stable to longwave disturbances everywhere. Liu (1999b) reported that the ray path of the *A*-mode could not be calculated in the southwestern region of the gyre because the longwave is unstable there. As noted above, however, the waves in the ventilated zone are unlikely to propagate into the shadow zone in which the longwaves are unstable as will be shown in Section 4d, so that this seems to suggest that the southwestern region of the ventilated zone could be unstable. It should also be noted that the potential vorticity gradients in the upper and the second layers are

opposite to each other in the southern half of the ventilated zone. Therefore, it is important to study the stability of the ventilated zone in the present model.

Since the wave is unstable when $(d_{11} - d_{22})^2 + 4d_{12}d_{21}$ in (3.3) is negative, we check if there is φ satisfying

$$(d_{11} - d_{22})^2 + 4d_{12}d_{21} = 0. \tag{3.17}$$

If there is no φ satisfying this equation, waves with any φ will be stable at that location, since there are always stable solutions. Eq. (3.17) can be rewritten as

$$[(a_{11} - a_{22})^2 + 4a_{12}a_{21}]k^2 + 2[(a_{11} - a_{22})(b_{11} - b_{22}) + 2(a_{12}b_{21} + a_{21}b_{12})]k + [(b_{11} - b_{22})^2 + 4b_{12}b_{21}] = 0, \tag{3.18}$$

where $k = \tan\varphi$ and a_{ij} and b_{ij} are (i, j)-components of matrices A and B. Therefore, if

$$J = [(a_{11} - a_{22})(b_{11} - b_{22}) + 2(a_{12}b_{21} + a_{21}b_{12})]^2 - [(a_{11} - a_{22})^2 + 4a_{12}a_{21}][(b_{11} - b_{22})^2 + 4b_{12}b_{21}] < 0, \tag{3.19}$$

there is no real k satisfying (3.19), and hence the waves are stable. Using (A.3), (A.4) and (2.5) in (3.19), we obtain

$$J = -\frac{4\beta^2\gamma_1\gamma_2^2}{f_1 f^2}\left(\frac{1}{f} - \frac{1}{f_1}\right)\left\{\gamma_1\left(\frac{1}{f} - \frac{1}{f_1}\right)^2 + \frac{\gamma_2}{f^2}\right\}H^2\left(\frac{\partial H}{\partial x}\right)^2, \tag{3.20}$$

after tedious manipulation. Since $f < f_1$, J is negative everywhere, and hence the ventilated zone in the 2.5-layer model is stable to longwaves at least when the outcrop line is zonal. The result obtained here contrasts with that in a two layer model in which any vertical shear flow is unstable to a longwave disturbance (see, Pedlosky, 1987). The stability to shortwave disturbances will be addressed in Section 5.

d. Shadow zone

The most important result for the shadow zone is that the shadow zone is unstable to longwave disturbances. Substituting $H = H_0$ (= constant) into (3.5), we obtain

$$(d_{11} - d_{22})^2 + 4d_{12}d_{21} = \frac{\beta}{f^2}\cos\varphi\left\{\frac{\beta}{f^2}P_1^2\cos\varphi + 4\gamma_1\gamma_2 H_1\hat{\mathbf{z}}\cdot(\mathbf{K}\times\nabla(H_2/f))\right\} \tag{3.21}$$

If $(\partial/\partial x)(H_2/f) \neq 0$, this term changes sign at $\varphi = \pi/2$ and $3\pi/2$. In the shadow zone, $(\partial/\partial x)(H_2/f) = -f^{-1}(\partial/\partial x)H_1$ is positive, so that the instability occurs on the side of φ smaller than $\pi/2$ (or $3\pi/2$). An example of the dispersion relation is shown in Figure 7 (at location C in Fig. 1). The instability is caused by coupling of two modes (Fig. 7a), and the phase shift between η_1 and η_2 is seen (Fig. 7c). The dependence on wavelength of this instability and the maximum growth rate will be addressed in Section 5.

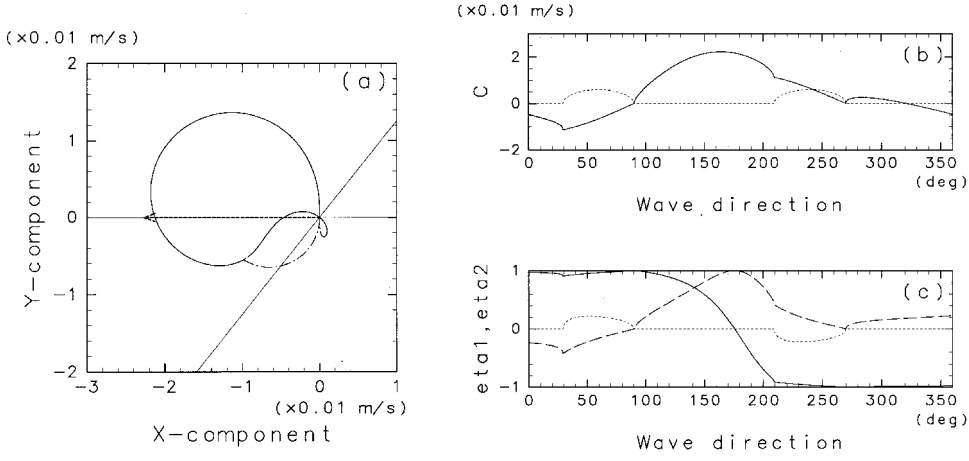

Figure 7. Eigenvalue solution in the shadow zone (location C in Fig. 1: longitude = 58°, latitude = 25°) as a function of the direction of the wavenumber vector: (a) two-dimensional diagram of phase velocity vector, (b) eigenvalue $c(\varphi)$ and (c) eigenvectors (vertical structure). In panel (a), at the portion denoted by the dash-dotted line, the eigenvalue c is complex. The westward dotted arrow is the group velocity without the basic flow. In panel (b), the dotted line denotes the imaginary part of c. In panel (c), the solid, dashed, and dotted lines denote η_1, the real part of η_2 and the imaginary part of η_2, respectively, where η_1 is assumed to be real and their amplitudes are normalized as satisfying $\sqrt{|\eta_1|^2 + |\eta_2|^2} = 1$.

e. Forced waves

In the present system, the two wave modes cannot completely be separated. This suggests that the forced wave response will be different from that in the resting ocean, in which the vertical wave modes are independent of each other. In this section, we study how the waves respond to w_e- and w_d-forcings.

As discussed in Appendix B, steady w_e-forcing generates only the stationary N-mode whose crest extends westward, while steady w_d-forcing forces only the stationary A-mode, whose crest extends southward along the second layer basic flow. This result is consistent with that expected from the steady ventilated thermocline model (see Huang and Pedlosky, 1999; and see also Appendix C). In addition, the stationary N-mode in the ventilated zone appears mainly in η_2 and has a barotropic structure, i.e., $\eta_1/\eta_2 = H_1/H$, while the stationary A-mode appears mainly in η_1 and has a baroclinic structure, i.e., $\eta_1/\eta_2 = -H/H_1$ (Fig. 4b and Appendix B).

Figure 8 depicts the temporal evolution of η_1 and η_2 when the steady w_e-forcing with the following form is applied for $t \geq 0$:

$$w_e = -\frac{|c_1|\hat{\eta}}{L} \exp\{-(x^2 + y^2)/r_0^2\}, \tag{3.22}$$

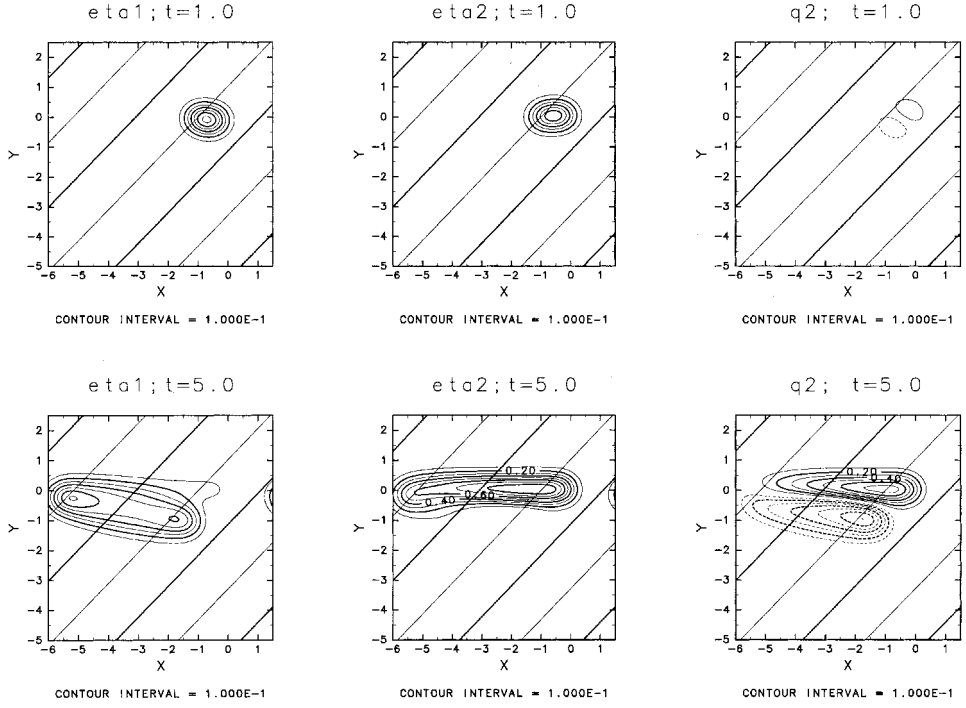

Figure 8. Temporal evolution of disturbance generated by w_e-forcing which is turned on at $t = 0$ in the ventilated zone (location B in Fig. 1): η_1 (left column), η_2 (middle column) and $\eta_2 - \eta_1$ (right column). The amplitude is normalized by $\hat{\eta}$ in (3.22), and contour intervals are denoted below each panel.

where $\hat{\eta}$ is the scale of the magnitude of η_1 and η_2, c_1 is the speed of the first baroclinic mode defined by (3.14), L is the horizontal length scale and $r_0 = 2.5L$. The time, t, is normalized by $L/|c_1|$ as well. The initial condition is $\eta_1 = \eta_2 = 0$.

Since the steady state is reached soon in the forcing region, the stationary N-mode, which mainly appears in η_2, extends westward directly from the forcing region (see the middle column in Fig. 8). We can, however, see a large amplitude disturbance in η_1 as well (see the left column in Fig. 8). This disturbance does not extend from the forcing region but from the western edge of the disturbance mainly seen in η_2 (N-mode). Whereas the N-mode has a barotropic structure ($\eta_1\eta_2 > 0$), the disturbance mainly seen in η_1 has a baroclinic structure ($\eta_1\eta_2 < 0$).

The reason why the A-mode is generated at the western edge of the N-mode is illustrated in Figure 9. Since negative w_e-forcing corresponds to water supply only to the upper layer, the upper layer mass increases while the second layer mass is conserved (see the left graph in Fig. 9a). In the stationary N-mode generated directly by w_e, however, η_1 is much smaller than η_2 (see Fig. 4b), so that only the vertical structure of the stationary N-mode (the middle graph in Fig. 9a) cannot satisfy the total mass budget, and the A-mode must be

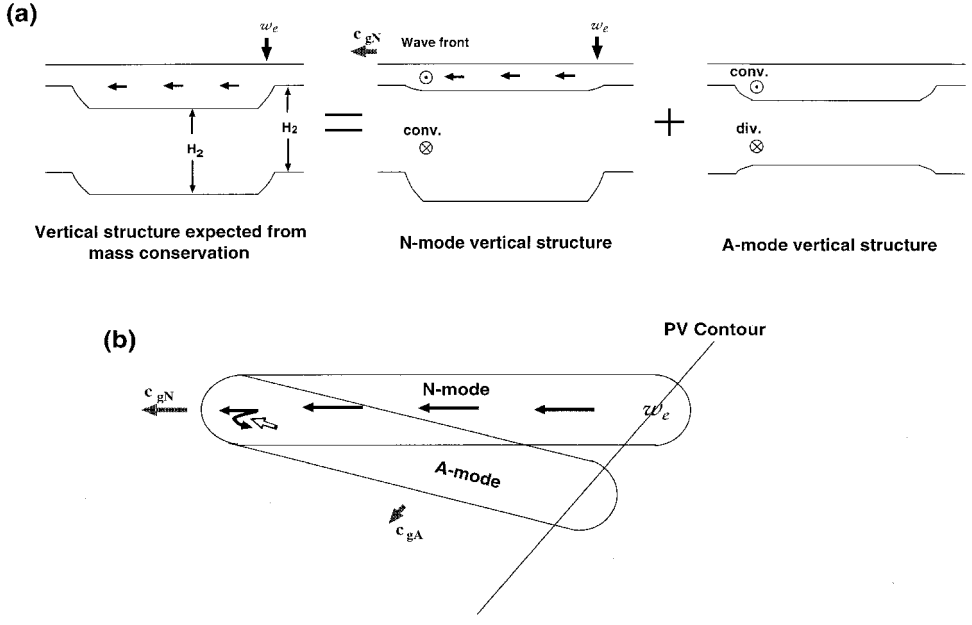

Figure 9. Schematic diagram for explaining the reason of *A*-mode generation at the western edge (wave front) of the forced *N*-mode: (a) side view, and (b) plane view. The solid arrows denote the upper layer mass flux, the symbols ⊙ and ⊗ in (a) denote the mass flux from the *N*-mode to the *A*-mode and the *A*-mode to the *N*-mode respectively, and the open arrow in (b) denotes the direction of the second layer mass flux.

generated (the right graph). The water supplied by w_e flows westward, and the westward flow converges at the *N*-mode wave front. The westward mass flux, $\int w_e dx$, however, is much larger than the propagation speed of the *N*-mode front multiplied by the amplitude, $c_{gN}\eta_1$, because of small η_1. In the second layer, large water convergence is necessary at the *N*-mode wave front since $\eta_2 \gg \eta_1$. These mass imbalances at the *N*-mode wave front excite an *A*-mode which has large positive η_1 and small negative η_2. Therefore, when w_e-forcing is applied, a large temperature anomaly in the upper thermocline inevitably occurs south of the forcing latitude, while the large temperature anomaly in the lower ventilated thermocline is limited only to the forcing latitude. This result contrasts with that in a resting ocean; when the ocean is at rest, the effect of the w_e-forcing can be seen only within the forcing latitude, even in the transient stage.

When w_d-forcing with the same spatial distribution as in (3.22) is applied, a similar phenomenon occurs (see Fig. 10). The negative w_d-forcing transfers the water mass from the upper layer to the second layer, and total mass is conserved. In the forcing region, the stationary *A*-mode responds. Although $|\eta_1| \gg |\eta_2|$ for the stationary *A*-mode, η_2 is not negligible and is positive when w_d is negative. This means that the total mass cannot be conserved only by the stationary *A*-mode. Therefore, the *N*-mode is generated at the southwestern edge of the *A*-mode, although its signal is weak.

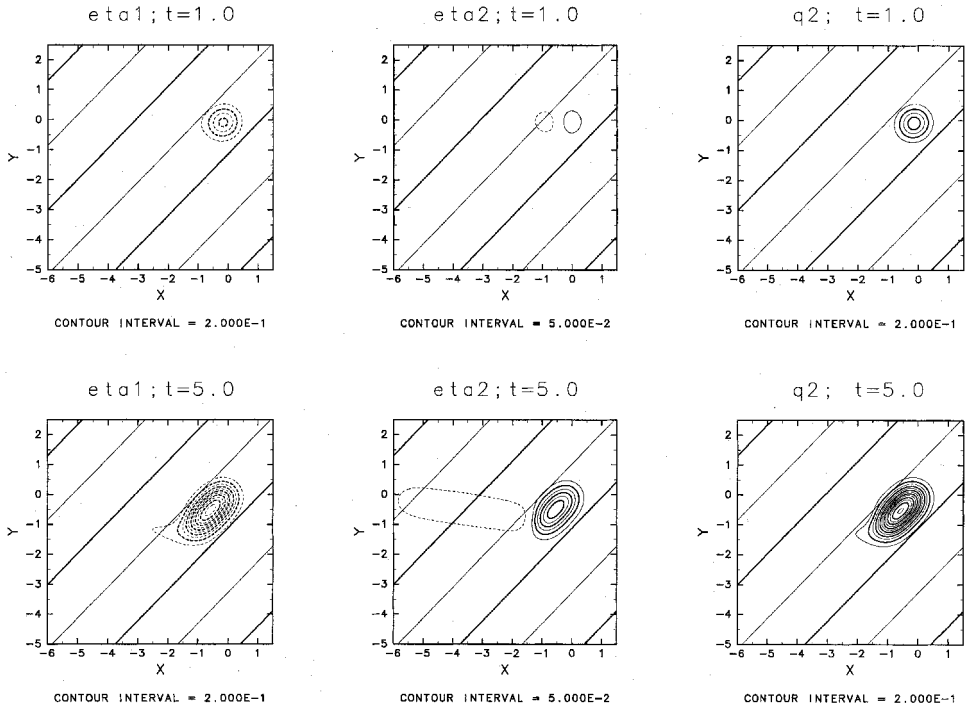

Figure 10. Same as Figure 8 but for w_d-forcing.

In the RY pool, the characteristics of steady response are similar to those in the ventilated zone; only the N-mode responds to a steady w_e-forcing, and only the A-mode responds to a steady w_d-forcing. However, in the RY pool, w_e-forcing only generates the N-mode, even in the transient stage (not shown), since the N-mode satisfies the relation $\eta_1 = \eta_2$. On the other hand, the response to w_d-forcing is similar to that in the ventilated zone (not shown); a weak N-mode is radiated at the southwestern edge of the A-mode signal.

4. Propagation in an oceanic gyre

So far, we have studied the wave dynamics based on the local eigenvalue solution and numerical computations with constant coefficients A and B. In the present section, we discuss the gyre-scale wave dynamics.

a. Wave properties and steady solutions

We have defined the typical group velocity and the typical vertical structure of each mode in Section 3c, and shown that they agree well with the propagation speeds of the

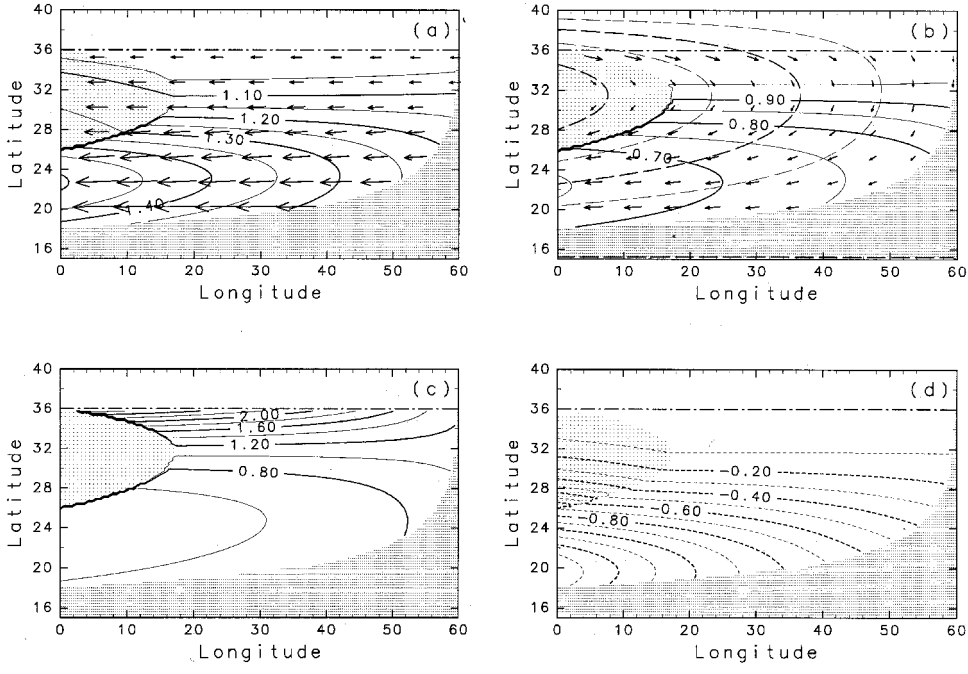

Figure 11. Gyre scale distribution of wave properties: (a) typical group velocity of the *N*-mode, (b) typical group velocity of the *A*-mode, (c) typical vertical structure, η_2/η_1, of the *N*-mode, and typical vertical structure of the *A*-mode. Solid contours in (a) and (b) are the ratios of the group velocities to c_1 and the second layer advection speed, respectively. The dashed contours in (b) are the second layer stream lines, P_2.

locations of maximum η_2 and maximum η_1 and the vertical structures. We examine the gyre scale distributions of these properties before discussing the wave propagation.

Figures 11(a) and (b) depict the distributions of the *N*-mode typical group velocity vectors. The contours in Panel (a) denote the ratio of the absolute value of the *N*-mode typical group velocity, $|\mathbf{c}_{gN}|$, to that of the first baroclinic mode in the resting ocean, c_1, defined by (3.14). In the RY pool, the ratio c_{gN}/c_1 is unity for $H_1 = 0$ and takes a maximum for $H_1/H_2 = 0.5$ when $\gamma_1 = \gamma_2$ (compare (3.14) with (3.13)). This tendency holds in the ventilated zone as well. Since H_1/H_2 increases southward in the present model, c_{gN}/c_1 increases southward. Around 23N, H_1/H_2 becomes 0.5, so the maximum occurs there. Furthermore, in the ventilated zone, advection by the second layer current is also important (see Appendix B). Killworth *et al.* (1997) showed that the ratio is smaller in the lower latitude, based on the observed ocean density field. The difference from their result must come from the difference between the density structures in the 2.5-layer ventilated thermocline model and in the real ocean. The potential vorticity distribution in unventilated layers may also be important for the wave propagation in the real ocean. On the other hand, the vectors in panel (b) imply that the *A*-mode typical group velocity is almost along the

second layer pressure contours (dashed lines), but it is smaller than the advection velocity: only 70% in the southwestern region (the solid contours represents the ratio of the A-mode typical group velocity to the advection velocity).

The gyre scale distribution of the typical vertical structure, η_2/η_1, is depicted in Figures 11(c) and (d). For the N-mode, η_2/η_1 is almost unity in the central to the southern region, and is unity in the RY pool as demonstrated in Section 3b. This means that the typical N-mode wave has only a small potential vorticity anomaly in the second layer even in the ventilated zone. On the other hand, η_2/η_1 of the A-mode is almost zero near the outcrop latitude, while its magnitude is nearly unity in the southwestern region.

Since we will discuss the response to atmospheric forcing in Section 4c, we outline the steady solutions as well (for details, see Appendix C). The following summary is only for the RY pool and the ventilated zone, because the shadow zone is unstable as mentioned in Section 3d.

1. The amplitudes, $|\eta_1|$ and $|\eta_2|$, of the N-mode decrease westward because of the increases of H_1 and H_2.
2. The amplitude, $|\eta_1|$, of the A-mode decreases southward, while $|\eta_2|$ is almost unchanged and increases slightly north of a certain latitude. The increase of $|\eta_2|$ means that the difference between the perturbed stream lines and the basic stream lines increases southward in the second layer.
3. The potential thickness anomaly in the second layer, $(\eta_2 - \eta_1)/f$, is not conserved along the basic state stream lines in the ventilated zone. This is because the path of a fluid particle changes; the path shifts eastward for positive potential thickness anomaly and westward for negative potential thickness anomaly.
4. The N-mode solution is discontinuous at the internal boundary between the ventilated zone and the RY pool, since the vertical structure of the stationary N-mode is different in these two zones. This discontinuity is significant in η_1 because $H \gg H_1$, and is canceled by the change in the position of the internal boundary.

b. Free wave propagation

Figure 12 shows the temporal evolution of an initial disturbance given by

$$\eta_1 = \eta_0 \exp\{-[(x - x_0)^2 + (y - y_0)^2]/r_0^2\}, \quad \eta_2 = 0 \tag{4.1}$$

where (x_0, y_0) is set to be longitude 45° and latitude 30°, $(x, y) = (a\lambda \sin\theta, a\theta)$ and $r_0 = 250$ km. The initial disturbance disperses into two parts, one of which resembles the N-mode and the other the A-mode. The bridges connecting these parts are also seen. Figure 13(a) shows the trajectories of the maximum η_1 and the maximum η_2 ($\eta_{1\max}$ and $\eta_{2\max}$, hereafter) with the trajectories calculated by the N-mode and A-mode typical group velocities, and those calculated by c_1 and the group velocity of the stationary A-mode. The trajectory calculated from the N-mode typical group velocity (□) does not start at the

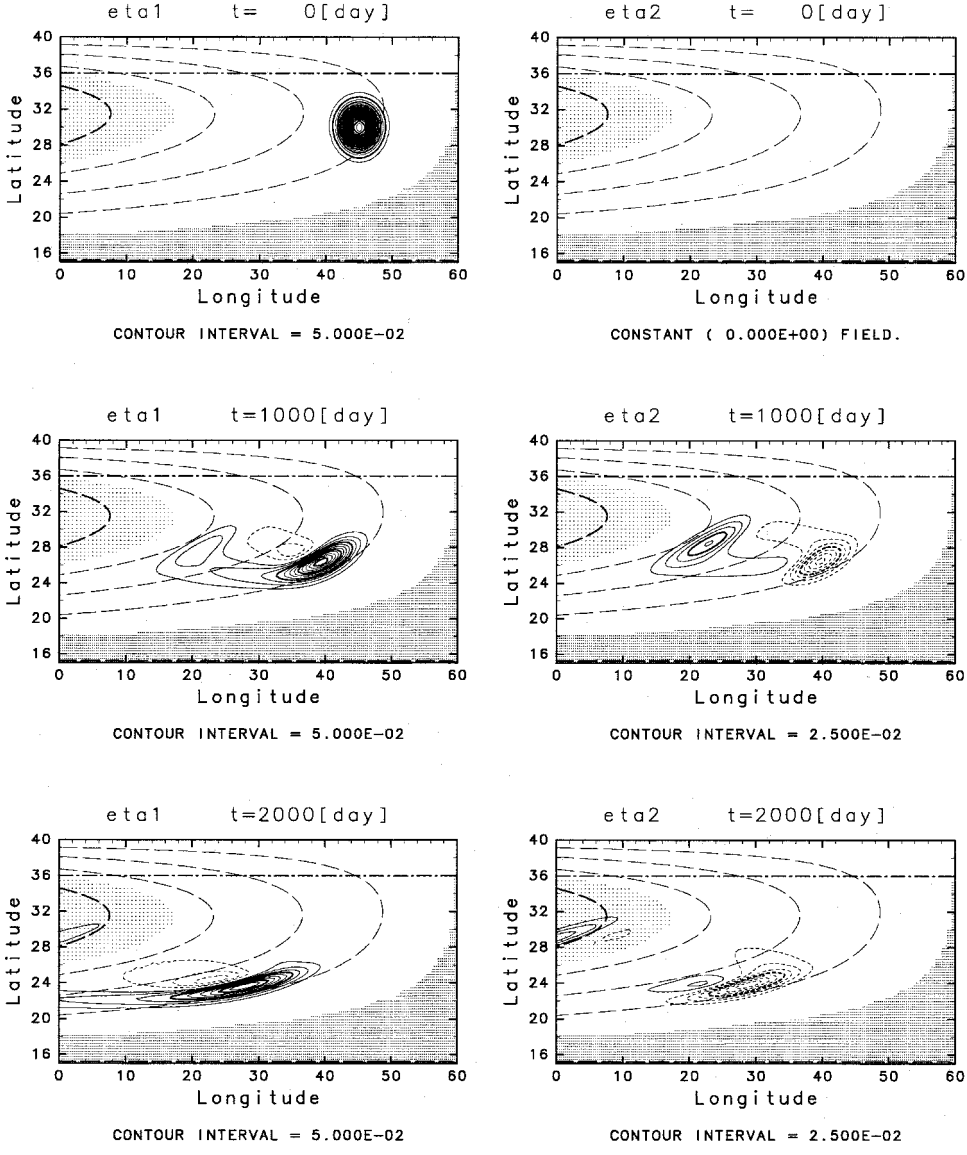

Figure 12. Gyre-scale evolution of an initial disturbance given only in η_1: η_1 (left column) and η_2 (right column). The amplitude is normalized by that of the initial disturbance, and contour intervals are denoted below each panel.

center of the initial disturbance but was chosen as the N-mode trajectory fits the η_{2max} trajectory. The η_{2max} trajectory (+) agrees well with that calculated from the N-mode typical group velocity (□). The propagation velocity has a southward component in the ventilated zone and is purely westward in the RY pool, and is larger than c_1(◇). The

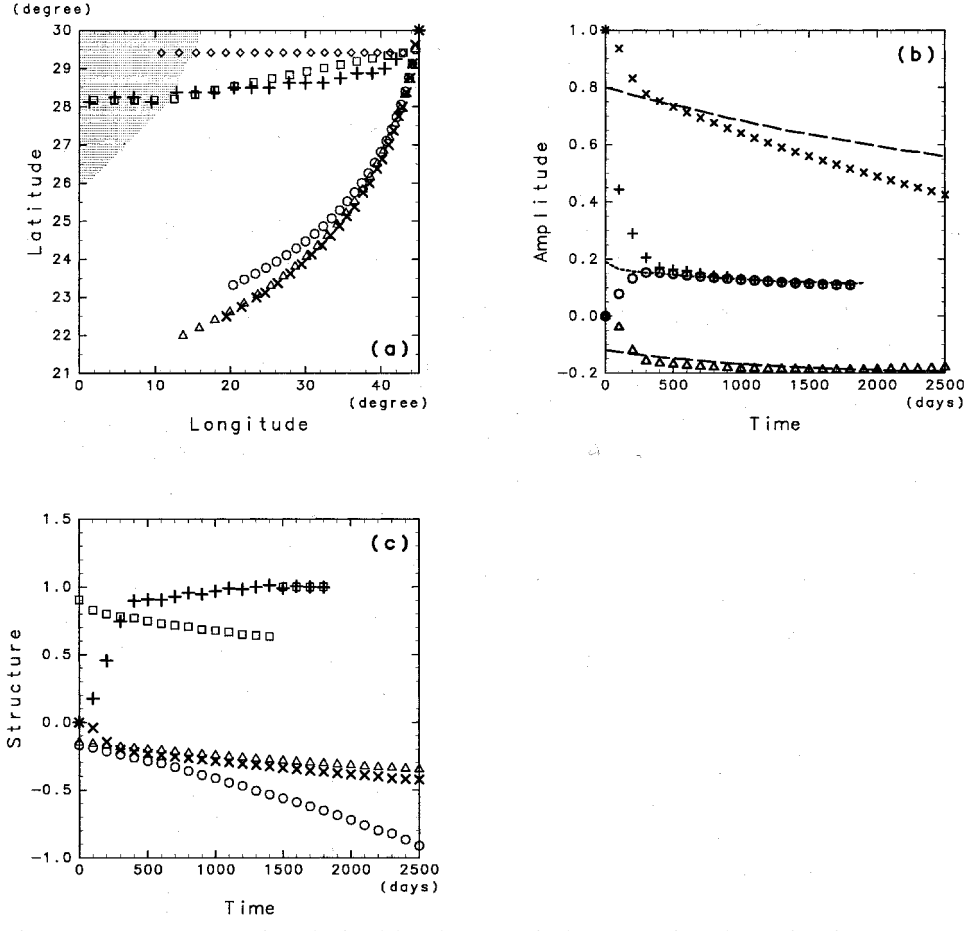

Figure 13. Wave properties obtained by the numerical computation shown in Figure 12: (a) trajectories of η_{1max} ($\times$) and η_{2max} ($+$), (b) η_1 and η_2 at η_{1max} ($\times$, $\triangle$) and at η_{2max} ($+$, $\bigcirc$), and (c) vertical structures, η_2/η_1 at η_{1max} ($\times$) and η_{2max} ($+$). In panel (a), trajectories calculated by the typical A-mode group velocity ($\bigcirc$), the typical N-mode group velocity ($\square$), the stationary A-mode group velocity ($\triangle$) and c_1 ($\diamond$) are also plotted, and the shade denotes the RY pool. The dashed lines in panel (b) are amplitudes calculated by (C.12) using f at the location of η_{1max}; the dotted line is proportional to $1/H$ in the ventilated zone and to $1/P_1$ in the RY pool calculated by H and P_1 at the location of η_{2max}. In panel (c), η_2/η_1 of the typical A-mode ($\bigcirc$) and the stationary A-mode ($\triangle$) at the location of η_{1max} and that of typical N-mode ($\square$) at the location of η_{2max} are also plotted.

trajectory of η_{1max} ($\times$) also agrees well with that calculated from the A-mode typical group velocity ($\bigcirc$), although the A-mode typical trajectory is slightly displaced from that of η_{1max}; the trajectory of η_{1max} is rather strictly along the P_2 contour as is the trajectory calculated from the group velocity of the stationary A-mode ($\triangle$).

Figure 13(b) shows η_1 and η_2 at the locations of η_{1max} and η_{2max}. At the location of η_{1max}, η_1 ($\times$) is positive and η_2 ($\triangle$) is negative, and the amplitude of η_1 rapidly decays as it propagates, while that of η_2 is almost constant. This behavior is similar to the latitudinal dependence of the amplitude in the stationary *A*-mode (dashed line in Fig. 13b), although the change in η_1 is much larger than that of the stationary *A*-mode. The vertical structure, η_2/η_1, shows similar behavior of the stationary *A*-mode ($\triangle$ in Fig. 13c) as well, but not the typical *A*-mode ($\bigcirc$).

On the other hand, at the location of η_{2max}, η_1 and η_2 ($+$ and $\bigcirc$ in Fig. 13b) almost coincide with each other. Therefore, the vertical structure, η_2/η_1, (symbol, $+$, in Fig. 13c) slightly differs from that of the typical mode whose η_2/η_1 is less than unity in the ventilated zone ($\square$ in Fig. 13c). The amplitude decays gradually as it propagates westward (Fig. 13b). This amplitude decay must have been caused by the fourth term of (2.4), since the vertical structure (eigenvector) is almost unchanged. This suggests that each of (ζ_1, ζ_2) in (2.9) will be constant along the η_{2max} trajectory, since (2.9) does not have a term directly proportional to the amplitude of (ζ_1, ζ_2). The relation between (η_1, η_2) and (ζ_1, ζ_2) in the ventilated zone is

$$\begin{pmatrix} \eta_1 \\ \eta_2 \end{pmatrix} = \begin{pmatrix} \dfrac{f}{H}\zeta_1 \\ \dfrac{f}{H_1}\zeta_2 \end{pmatrix} = \begin{pmatrix} \dfrac{f}{H}\zeta_1 \\ \dfrac{ff_1}{(f_1 - f)H}\zeta_2 \end{pmatrix},$$

where (A.3) has been used. In the RY pool, since $\eta_2/\eta_1 = 1$ for the *N*-mode, ζ_2 must vanish. Therefore,

$$\begin{pmatrix} \eta_1 \\ \eta_2 \end{pmatrix} = \begin{pmatrix} \dfrac{\gamma_2 f}{P_1}\zeta_1 \\ \dfrac{\gamma_2 f}{P_1}\zeta_1 \end{pmatrix}.$$

If we assume that (ζ_1, ζ_2) are kept constant in each zone, η_js will be proportional to $1/H$ in the ventilated zone, but to $1/P_1$ in the RY-pool, since f is almost constant. The dotted line in Figure 13(b) shows that the amplitude change calculated here agrees well with the temporal evolution of the *N*-mode amplitude.

The cause of the differences between the typical wave properties and the numerical results could be interpreted by the horizontal structures of the disturbances (Fig. 12). Both the disturbances of η_{1max} and η_{2max} are elongated along the potential vorticity contours in the second layer. This suggests that the disturbances are dominated by the modes whose wavenumber is directed parallel to $\nabla(H_2/f)$. If we set $\mathbf{K} \times \nabla(H_2/f) = 0$ in (B.2), we can easily find that η_2/η_1 becomes unity for the *N*-mode, and the *A*-mode becomes the stationary *A*-mode. The group velocity of the stationary *A*-mode is along the P_2 contour and its vertical structure agrees well with that at the location of η_{1max}. The elongation of the disturbances is perhaps caused by the dependence of the group velocities on the latitude.

The magnitudes of the group velocities of both modes tend to increase southward (see Fig. 11), so that the N-mode crest inclines northeastward and the A-mode crest is stretched along the P_2 contour. The decay rate of η_1 at the location of $\eta_{1\max}$ is larger than that expected from the latitudinal dependence of the amplitude of the stationary A-mode as mentioned above. This could be caused by dispersion along the P_2 contour.

c. Forced wave responses

Figure 14 shows the temporal evolution when an anomalous Ekman pumping whose lateral distribution is the same as that in (4.1) is applied for $t > 0$. In this figure, the magnitude of anomalous Ekman pumping velocity is set to be -1.0×10^{-6} m/s. The N-mode disturbance which appears mainly in η_2 is generated in the forcing region and propagates westward. The A-mode is continuously generated at the wave front of the N-mode unless the N-mode wave front propagates into the RY pool. In the RY pool, because of zero potential thickness anomaly, further generation of the A-mode at the N-mode wave front does not occur. The stationary N-mode experiences a significant change at the internal boundary between the ventilated zone and the RY pool because the vertical structure in the RY pool is different from that in the ventilated zone. Since the potential thickness anomaly in the second layer in the RY pool is zero, the amplitude in η_1 increases at the internal boundary, and discontinuities in η_1 and η_2 occur. This discontinuity is canceled by the eastward shift of the internal boundary (see Appendix C).

As mentioned in Section 3e, although the steady response to the anomalous Ekman pumping is limited to the latitude band in which the forcing is applied, the A-mode signal appears in the southwestern region in the transient stage, causing a temperature anomaly in the upper thermocline there. The amplitude in η_1 of the A-mode signal decreases as it propagates southward, mainly because f decreases, but the signal will persist about ten years.

For w_d-forcing with the same lateral distribution, the solution is qualitatively the same as that in the local case in Section 3e, except for the latitudinal dependence of the amplitude (Fig. 15). The A-mode signal extends southwestward along the second layer stream lines of the basic state. The amplitude in η_1 decreases southward significantly, while that in η_2 is almost constant and slightly increases near the forcing region as mentioned in Appendix C. Although the N-mode is generated at the wave front of the A-mode, its amplitude is small.

5. Dependence on the wavelength

So far, only the longwave disturbances have been discussed. In this section, we study the dependence of the local wave properties on the wavelength. As mentioned in Section 3a, the treatment in Section 3 is the same as the longwave approximation in the quasi-geostrophic model, and the inclusion of the relative vorticity is a rather easy task. The linearized quasi-geostrophic equations can be written as

$$\frac{\partial q_j}{\partial t} + U_j \frac{\partial q_j}{\partial x} + V_j \frac{\partial q_j}{\partial y} + u_j \frac{\partial}{\partial x}\frac{H_j}{f} + v_j \frac{\partial}{\partial y}\frac{H_j}{f} = 0, \tag{5.1}$$

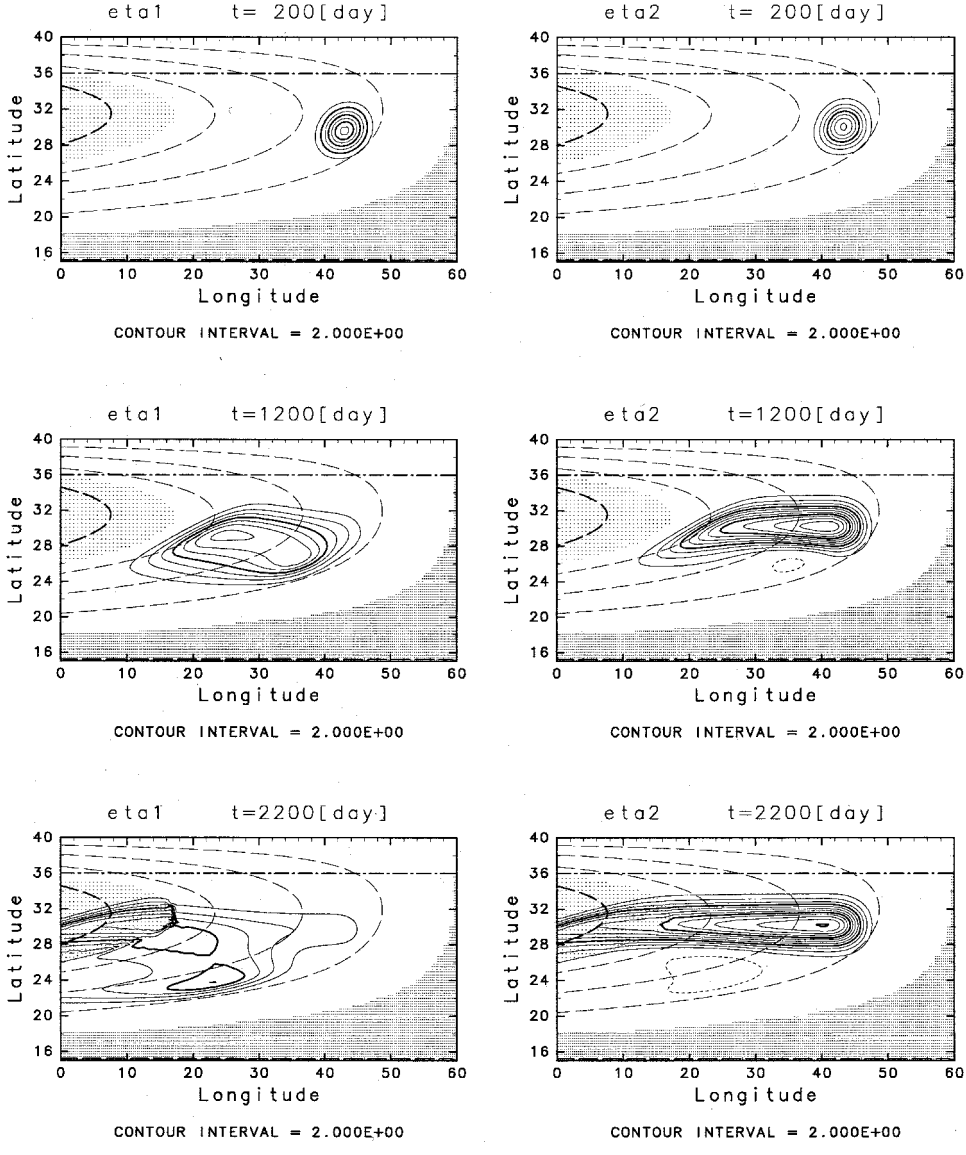

Figure 14. Gyre-scale evolution of disturbances generated by w_e-forcing which is turned on at t = 0: η_1 (left column), η_2 (right column). The forcing has the same lateral structure as the initial disturbance in Figure 11, and the magnitude of the forcing is 10^{-6} m s^{-1}. The contour intervals [unit is m] are denoted below each panel.

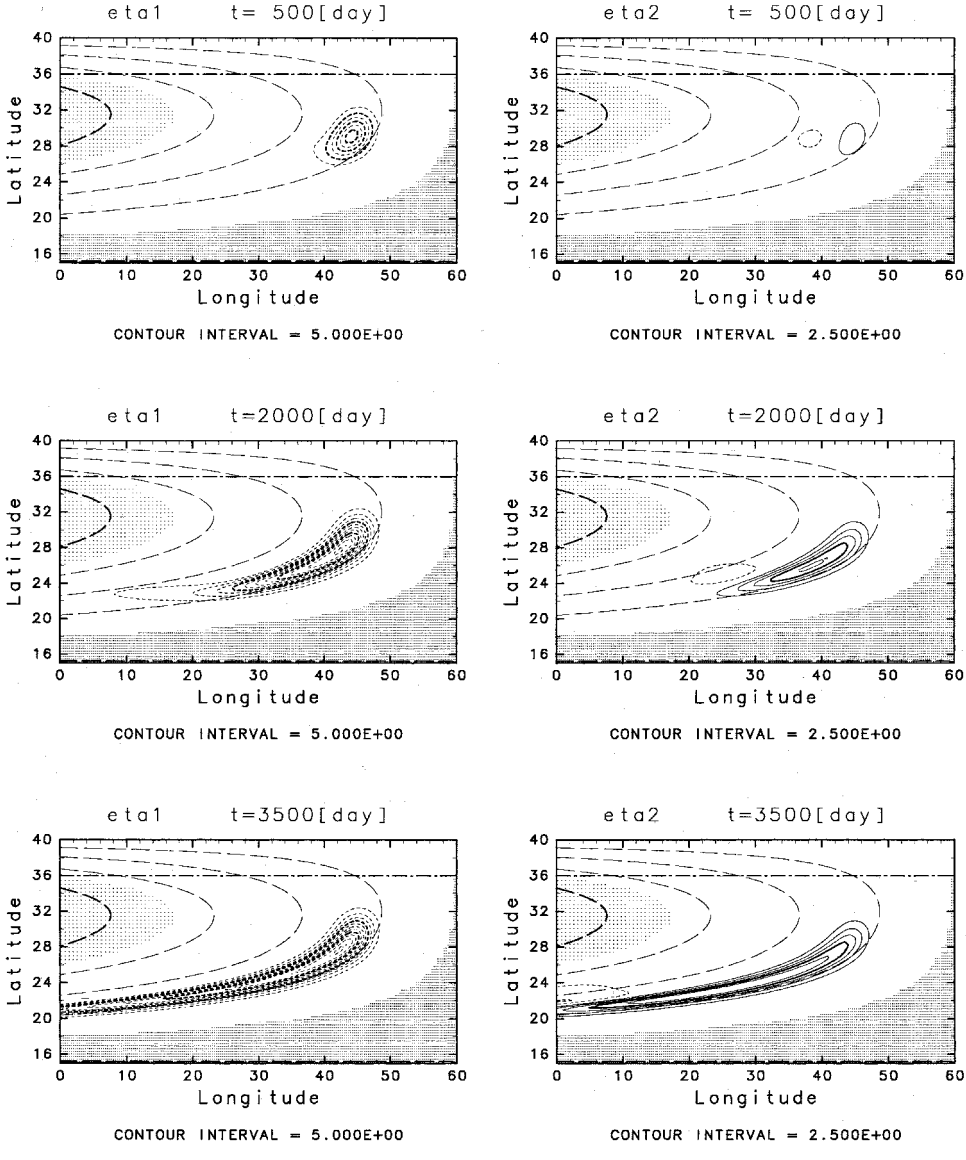

Figure 15. Same as Figure 14 but for w_d-forcing.

where $j = 1, 2$ and

$$q_1 = \frac{1}{f}\left\{\eta_1 - \frac{H_1}{f^2}\left[\gamma_1\nabla^2\eta_1 + \gamma_2\nabla^2(\eta_1 + \eta_2)\right]\right\}, \tag{5.2}$$

$$q_2 = \frac{1}{f}\left\{\eta_2 - \eta_1 - \frac{H_2}{f^2}\gamma_2\nabla^2\eta_2\right\}, \tag{5.3}$$

are the quasi-geostrophic potential vorticities multiplied by $-H_j/f^2$ (potential thicknesses) in which f and H_j are treated as constants, and the other variables and parameters are the same as in previous sections. Considering the plane wave solution, $(\eta_1, \eta_2) = (\hat{\eta}_1, \hat{\eta}_2)\exp\{i(kx + ly - \sigma t)\}$, (5.1) can be rewritten in a matrix form:

$$-\sigma \mathsf{M}\begin{pmatrix} \hat{\eta}_1 \\ \hat{\eta}_2 \end{pmatrix} + \mathsf{D}_\mathsf{K}\begin{pmatrix} \hat{\eta}_1 \\ \hat{\eta}_2 \end{pmatrix} = 0. \tag{5.4}$$

where

$$\mathsf{M} = \begin{pmatrix} 1 + \dfrac{H_1}{f^2}\gamma_1|\mathbf{K}|^2 & \dfrac{H_1}{f^2}\gamma_2|\mathbf{K}|^2 \\ -1 & 1 + \dfrac{H_2}{f^2}\gamma_2|\mathbf{K}|^2 \end{pmatrix}, \tag{5.5}$$

$$\mathsf{D}_\mathsf{K} = \begin{pmatrix} (kU_1 + lV_1)m_{11} + \gamma_1\hat{\mathbf{z}} \cdot \left(\mathbf{K} \times \nabla\left(\dfrac{H_1}{f}\right)\right) & (kU_1 + lV_1)m_{12} + \gamma_2\hat{\mathbf{z}} \cdot \left(\mathbf{K} \times \nabla\left(\dfrac{H_1}{f}\right)\right) \\ (kU_2 + lV_2)m_{21} & (kU_2 + lV_2)m_{22} + \gamma_2\hat{\mathbf{z}} \cdot \left(\mathbf{K} \times \nabla\left(\dfrac{H_2}{f}\right)\right) \end{pmatrix}. \tag{5.6}$$

Here $\mathbf{K} = (k, l)$ and m_{ij} is the (i, j)-component of M. The eigenvalue of the matrix $\mathsf{M}^{-1}\mathsf{D}_\mathsf{K}$ gives the frequencies, σ, as functions of k and l. Although one set of (k, l) gives two frequencies, σ_1 and σ_2, we only consider one of them, because $\sigma_1(k, l) = -\sigma_2(-k, -l)$ as noted in Section 3a. The phase speed (the real part of $\sigma/\sqrt{k^2 + l^2}$), group velocity and the growth rate (imaginary part of σ) are shown in Fig. 16 for each location A, B and C denoted in Figure 1.

In the RY pool (location A), the A-mode is nondispersive and its group velocity always coincides with the second layer advection velocity (shaded region in Fig. 16a), while the N-mode phase speed decreases with the wavenumber. The phase speeds of these modes coincide with each other around the wavelength of 100 km, but no instability occurs because of zero potential vorticity gradient in the second layer.

As proved in Section 3c, the ventilated zone is stable to longwave disturbances, but not to disturbances with finite wavelength. The A-mode in the ventilated zone is weakly dispersive, while the N-mode phase speed decreases with wavenumber as in the RY pool. The phase speed of the westward propagating N-mode with wavelength of 628 km is 91% of that of the N-mode longwave at location B. As the wavenumber increases, the phase speeds of the two modes become closer to each other, and instability occurs around the wavelength of 200 km. This instability is of course a baroclinic instability. The e-holding time scale of maximum unstable growth is 120 days and its wavelength is 110 km.

In the shadow zone, longwaves are unstable as proven in Section 3c. The growth rate increases with wavenumber. The wavelength giving the maximum growth rate at location C is about 130 km, and its e-holding time scale is 40 days.

The gyre scale distributions of wave properties are depicted in Figure 17. It can be seen

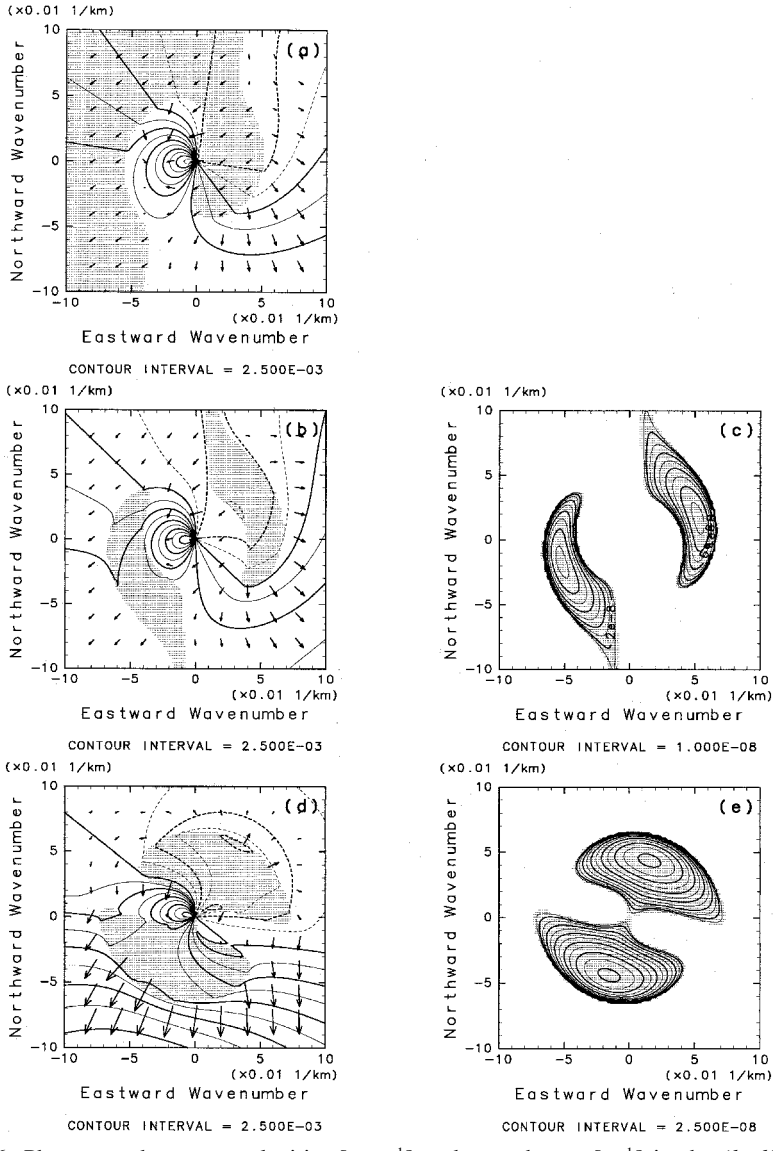

Figure 16. Phase speeds, group velocities [m s^{-1}] and growth rate [s^{-1}] in the (k, l) plane at locations A (RY pool), B (ventilated zone) and C (shadow zone) in Figure 1b: (a) phase speed (contour) and group velocity (arrow) at location A where the waves are stable, (b) phase speed (contour) and group velocity (arrow) at location B, (c) growth rate at location B, (d) phase speed (contour) and group velocity (arrow) at location C, (e) growth rate at location C. Shade in (a) denotes the region where the wave is non-dispersive (group velocity coincides with the second layer current velocity), and the shade in the other panels denotes the unstable region.

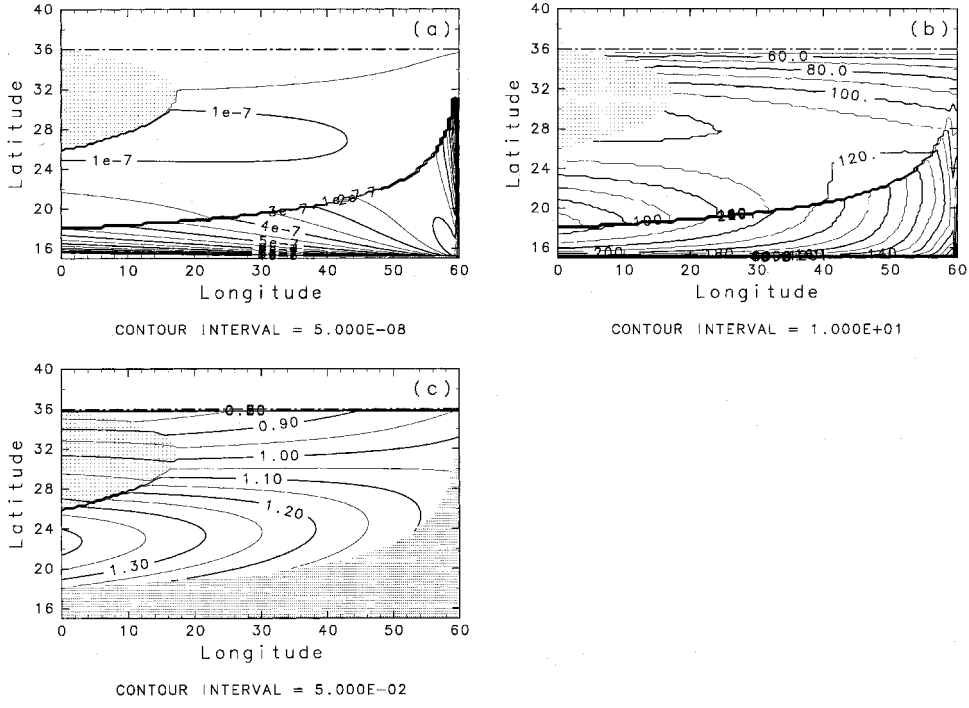

Figure 17. Gyre-scale distributions of wave properties with finite wavelength: (a) maximum growth rate [s^{-1}], (b) wavelength of the most unstable wave [km], and (c) westward phase speed of the N-mode with 628 km wavelength relative to c_1.

in panels (a) and (b) that the instability in the shadow zone is much stronger than that in the ventilated zone, and the wavelength of the most unstable wave in the ventilated zone is much shorter (around 100 km) than that in the shadow zone (around 200 km). In the shadow zone, the growth rate is large near the eastern and southern boundaries, while that in the ventilated zone is large in the center of the gyre. The dispersive nature of the N-mode reduces the westward phase speed even in waves with the wavelength of several hundred km, e.g., $k = 1/100$ km (wavelength is 628 km) as discussed above. In the southern subtropical gyre, however, the westward phase speed is still higher than c_1, as shown in panel (c).

6. Summary

In the present article, we have investigated the linear planetary wave dynamics in a 2.5-layer version of the LPS model. First, we have considered longwave disturbance under the assumption that the horizontal scale is much shorter than the gyre scale. Second, the gyre scale propagation of disturbances has been considered, and finally, we have briefly

discussed the effects of finite wavelength on the local wave properties. The main results are summarized as follows:

1. The shadow zone is baroclinically unstable while the ventilated zone is stable to long-wave disturbances, at least when the outcrop line is zonal.

2. Local eigenvalue analysis has confirmed that there are two modes as discussed by Liu (1999a,b); one of them (the N-mode) has a barotropic structure and has strong westward propagation tendency, and the other (the A-mode) mainly has a baroclinic structure and tends to propagate along the second layer basic flow.

3. In the ventilated zone, the N-mode and the A-mode are dispersive, and the vertical structure depends on the wave direction. We introduce a typical group velocity and typical vertical structure for each mode. The typical group velocity of the N-mode is directed almost westward, but slightly southward, and its magnitude is larger than the group velocity of the first baroclinic mode in a resting ocean. The typical group velocity of the A-mode is directed almost along the second layer current and its magnitude is smaller than the advection velocity. These typical wave properties can interpret well the propagation of an initially compact disturbance in the local model.

4. When w_e-forcing is applied, the N-mode is generated. In the ventilated zone, although steady w_e-forcing only generates the stationary N-mode which extends westward, the wave front of the N-mode generates the A-mode which yields a significant anomaly in the upper layer depth south of the N-mode crest. For w_d-forcing, the A-mode is generated in the forcing region, and propagates southward along the second layer pressure contour, generating the N-mode at the wave front similar to the w_e-forcing case.

5. Free waves in a linearized planetary geostrophic model behave similarly to those in the local model. A detailed examination, however, shows some differences from the local case. In the planetary geostrophic case, both the disturbances appearing in mainly η_1 and in η_2 tend to be dominated by wave modes whose wavenumber vector is parallel to the second-layer potential vorticity gradient. The amplitude decay of the N-mode is proportional to $1/H$ in the ventilated zone and to $1/P_1$ in the RY-pool. When w_e-forcing is applied in the ventilated zone, the N-mode crosses the internal boundary between the ventilated zone and the RY pool, and jumps in the interfacial depths occur there because the second layer potential vorticity anomaly cannot enter the RY pool.

6. Dependences of the local wave properties on the wavelength have also been examined. The N-mode westward phase speed decreases with wavenumber. The A-mode is weakly dispersive in the ventilated zone, but non-dispersive in the RY-pool. In the RY pool, the two modes do not interact with each other and there is no instability. In the ventilated zone, the two modes interact and instability occurs at a

finite wavelength. The instability in the ventilated zone is much weaker than that in the shadow zone where the longwave disturbance is also unstable.

The existence of rather strong instability in the shadow zone suggests that the second layer in the shadow zone might have a mean motion in a time-dependent nonlinear model because the second layer potential vorticity would be mixed by unstable waves. The instability in the ventilated zone is weak and is limited to shortwaves, so that it will not be very significant in the gyre-scale dynamics. In regard to the application to ocean climate, item 4 is important, because the A-mode generated at the N-mode wave front can cause significant warming/cooling south of the forcing latitude, and the A-mode signals would persist in the subtropical gyre within ten years or more.

Acknowledgments. The authors thank the two anonymous referees for their valuable comments. This work was financially supported by the Japanese Ministry of Education, Science and Culture, and the Japan Society for the Promotion of Science. The GFD-DENNOU Library was used for drawing the figures.

APPENDICES

A. Basic state

The basic state used in this paper is a 2.5-layer version of the LPS model (Luyten *et al.,* 1983). The domain is divided into three zones, and the solution in each zone can be written in terms of the Coriolis parameter, f, the Sverdrup function, $D_0^2(\lambda, \theta)$:

$$D_0^2(\lambda, \theta) = \frac{2f^2}{\beta\gamma_2} \int_{\lambda_e}^{\lambda} W_e(\lambda, \theta) a \cos\theta d\lambda, \tag{A.1}$$

and the given parameters: $H_0 = H(\lambda_e)$, $f_1 = f(\theta_1)$, and γ_1 and γ_2.

Rhines and Young pool

In this zone, the potential thickness in the second layer is fixed at the value of that at the intersection of the western boundary and the outcrop line.

$$H_2 = \frac{f}{f_1}[H_0^2 + D_0^2(\lambda_w, \theta_1)]^{1/2},$$
$$H_1 = \frac{\gamma_2}{\gamma_1 + \gamma_2}\left[-H_2 + \left\{\left(\frac{\gamma_1}{\gamma_2} + 1\right)(H_0^2 + D_0^2) - \frac{\gamma_1}{\gamma_2} H_2^2\right\}^{1/2}\right], \tag{A.2}$$

where λ_w is the longitude at the western boundary.

Ventilated zone

In this zone, the potential thickness in the second layer is determined at the outcrop latitude and is conserved along constant H.

$$H_1 = \left(1 - \frac{f}{f_1}\right) H, \quad H_2 = \frac{f}{f_1} H, \tag{A.3}$$

where

$$H = H_1 + H_2 = \left\{ \frac{\gamma_2 (H_0^2 + D_0^2)}{\gamma_1 \left(1 - \frac{f}{f_1} \right)^2 + \gamma_2} \right\}^{1/2}. \tag{A.4}$$

Shadow zone

In this zone, the $H = H_1 + H_2$ is fixed at the constant value H_0, since the second layer is at rest.

$$H_1 = \left(\frac{\gamma_2}{\gamma_1} D_0^2 \right)^{1/2}, \quad H_2 = H_0 - H_1. \tag{A.5}$$

B. Some details of the eigenvalue solutions

Using (2.5), the eigenvalue of matrix D can be written as,

$$c = \frac{1}{2} \left\{ -\frac{\beta}{f^2} P_1 \cos\varphi + \mathbf{U}_2 \cdot \mathbf{K} + \sqrt{\left(\frac{\beta}{f^2} P_1 \cos\varphi + \mathbf{U}_2 \cdot \mathbf{K} \right)^2 + \frac{4\beta\gamma_1\gamma_2}{f^2} H_1 \hat{\mathbf{z}} \cdot \left(\mathbf{K} \times \nabla \frac{H_2}{f} \right) \cos\varphi} \right\}, \tag{B.1}$$

where we have taken only the plus sign. The difference from the case with $|\nabla(H_2/f)| = 0$ in Section 3b arises from the last term in the square root of (B.1). This term can be rewritten as,

$$\frac{4\beta\gamma_1\gamma_2}{f^2} H_1 \hat{\mathbf{z}} \cdot \left(\mathbf{K} \times \nabla \frac{H_2}{f} \right) \cos\varphi = -\frac{4\beta\gamma_1\gamma_2}{f^2} H_1 |\nabla(H_2/f)| \sin(\varphi - \varphi_q) \cos\varphi. \tag{B.2}$$

where φ_q is the direction of $\nabla(H_2/f)$ ($\pi < \varphi_q < 3\pi/2$ in the northern half of the gyre and $\pi/2 < \varphi_q < \pi$ in the southern half). When only the plus sign is taken, the westward propagating N-mode is given by $\varphi = \pi$, and the A-mode propagating along H_2/f contours is given by $\varphi = \varphi_q + \pi/2$ in the north and by $\varphi = \varphi_q - \pi/2$ in the south. It should be noted that $\varphi = \varphi_q - \pi/2$ is anti-parallel to $\mathbf{U}_2$, hence $c < 0$ for the A-mode in the southern half of the gyre.

Wave propagation in the ventilated zone

First, let us consider the effect of $\nabla(H_2/f)$ (or the second layer potential vorticity gradient) on the westward propagating N-mode with $\varphi = \pi$. Since $\varphi_q > \pi$ in the northern half of the ventilated zone and $\varphi_q < \pi$ in the south, the term (B.2) is negative in the northern half and positive in the southern half. Therefore, the westward velocity of the N-mode in the southern half of the ventilated zone is higher than that in the RY pool, and lower in the northern half. On the other hand, since the φ derivative of the term (B.2) at $\varphi = \pi$ is positive everywhere in the ventilated zone, the direction with the maximum phase velocity of the N-mode shifts southward from westward.

In regard to the A-mode propagating along the second layer potential vorticity contour, $\sin(\varphi - \varphi_q)\cos\varphi$ is positive in the north and negative in the south. Since $c > 0$ in the north and $c < 0$ in the south, this means that the phase speed of the A-mode propagating in the direction of $\mathbf{U}_2$ is smaller than the advection speed. Since $\cos\varphi$ is a decreasing function of φ for $0 < \varphi < \pi/2$ (south) and is an increasing function for $3\pi/2 < \varphi < 2\pi$ (north), we can find that the direction of the fastest propagating A-mode shifts rightward from the direction of $\mathbf{U}_2$.

Stationary waves and steady response

From (B.1) or the condition that $d_{11}d_{22} - d_{12}d_{21} = 0$, we can easily find that the stationary wave solutions satisfy

$$\varphi = \frac{\pi}{2}, \quad \text{or } \varphi = -\tan^{-1}\frac{V_2}{U_2} \tag{B.3}$$

The eigenvectors of stationary waves become

$$\mathbf{R}_s = \begin{pmatrix} H_1 \\ H \end{pmatrix} \text{ for stationary } N\text{-mode } (\varphi = \pi/2), \tag{B.4}$$

$$\mathbf{R}_s = \begin{pmatrix} H \\ -H_1 \end{pmatrix} \text{ for stationary } A\text{-mode } (\varphi = -\tan V_2/U_2). \tag{B.5}$$

The group velocities of these modes are westward for the stationary N-mode, and southwestward along $\mathbf{U}_2$ for the stationary A-mode.

When we write a steady solution as

$$\begin{pmatrix} \eta_1 \\ \eta_2 \end{pmatrix} = \mathbf{R}_s\phi, \tag{B.6}$$

the equation of the amplitude ϕ for steady forcing $\mathbf{W}$ becomes

$$\mathbf{L}_s\mathsf{N}\mathbf{R}_s\frac{\partial\phi}{\partial n} = \mathbf{L}_s\mathbf{W}, \tag{B.7}$$

for each stationary mode, where $\mathbf{L}_s$ is the left eigenvector of D, n is the coordinate directed to $\varphi + \pi/2$ (perpendicular to s-coordinate), $\mathsf{N} = -\mathsf{A}\sin\varphi + \mathsf{B}\cos\varphi$ and $\mathbf{W} = {}^t(-w_e + w_d, -w_e)$. Since $L_s = (0, 1)$ for the stationary N-mode and $L_s = (1, -1)$ for the stationary A-mode, the steady w_e forcing excites only the stationary N-mode, while the steady w_d forcing excites only the stationary A-mode.

C. Steady solutions in oceanic gyre

Although we can derive the linear steady solutions from (2.9) with $\partial/\partial t = 0$, here we derive them by linearizing the nonlinear steady solution (A.2)–(A.4) to a perturbation. Since the stationary N-mode is generated by a w_e anomaly, we can obtain the perturbed interface depth, η_1 and η_2, corresponding to the stationary N-mode, by changing D_0^2 to $D_0^2 + \phi_N$, where ϕ_N is an anomaly of the Sverdrup function. On the other hand, since the

stationary A-mode is generated by the potential thickness anomaly without change in the total transport, we can obtain those for the stationary A-mode, by changing the second layer potential thickness functional relation, $H_2/f = Q_2(H)$, to $(H_2 + \eta_2 - \eta_1)/f = Q_2(H + \eta_2) + \phi_A(H + \eta_2)$, where $Q_2(H)$ denotes the functional relation between the second layer potential thickness and the second layer stream function H in the basic state, and ϕ_A is an anomaly of the potential thickness.

Rhines and Young pool

When we take ϕ_N into consideration, the Sverdrup relation becomes

$$\gamma_1(H_1 + \eta_1)^2 + \gamma_2(H + \eta_2)^2 = H_0^2 + D_0^2 + \phi_N, \tag{C.1}$$

where ϕ_N is a constant in the zonal direction, because we consider the N-mode wave far from the forcing region. Linearized version of (C.1) is

$$2\gamma_1 H_1\eta_1 + 2\gamma_2 H\eta_2 = \phi_N. \tag{C.2}$$

Since the stationary N-mode has no potential thickness anomaly in the second layer,

$$\eta_2 - \eta_1 = 0. \tag{C.3}$$

From (C.2) and (C.3), we obtain

$$\eta_1 = \eta_2 = \frac{\phi_N}{2[\gamma_1 H_1 + \gamma_2 H]}. \tag{C.4}$$

On the other hand, for the stationary A-mode, the potential thickness in the second layer is

$$\frac{1}{f}(H_2 + \eta_2 - \eta_1) = Q_2(H + \eta_2) + \phi_A(H + \eta_2). \tag{C.5}$$

Since the potential vorticity in the basic state, Q_2^{-1}, is constant in the RY-pool, the linearized version of this equation becomes

$$\frac{1}{f}(\eta_2 - \eta_1) = \phi_A(H). \tag{C.6}$$

From (C.2) with $\phi_N = 0$ and (C.6), we obtain

$$\eta_1 = -\frac{f\gamma_2 H}{\gamma_1 H_1 + \gamma_2 H}\phi_A(H), \quad \eta_2 = \frac{f\gamma_1 H_1}{\gamma_1 H_1 + \gamma_2 H}\phi_A(H). \tag{C.7}$$

f decreases southward, while H_1 increases. So, the latitudinal distributions of $|\eta_1|$ and $|\eta_2|$ are different. The amplitude in η_1 decreases southwestward, but that in η_2 slightly increases for $fH_w/f_1H > (1 + \gamma_2/\gamma_1) - \sqrt{(\gamma_2/\gamma_1)(1 + \gamma_2/\gamma_1)}$, where $H_w = H(\lambda_w, \theta_1)$. Since $H + \eta_2$ gives a perturbed stream line in the second layer and H increases westward, the positive η_2 means eastward shift of the stream line, and the southward increase in η_2

means that the difference between the stream lines in the basic state and the perturbed state increases southward.

Ventilated zone

For the stationary N-mode, since there is no potential thickness anomaly and $Q_2(H + \eta_2) = (H + \eta_2)/f_1$, the linearized potential thickness equation becomes

$$\frac{1}{f}(\eta_2 - \eta_1) = \frac{\eta_2}{f_1}. \tag{C.8}$$

From (C.2) and (C.8), we obtain

$$\eta_1 = \frac{(1 - f/f_1)\phi_N}{2[\gamma_1(1 - f/f_1)^2 + \gamma_2]H}, \quad \eta_2 = \frac{\phi_N}{2[\gamma_1(1 - f/f_1)^2 + \gamma_2]H}. \tag{C.9}$$

The amplitude decreases westward since H increases.

For the stationary A-mode, the potential thickness becomes

$$\frac{1}{f}(H_2 + \eta_2 - \eta_1) = \frac{1}{f_1}(H + \eta_2) + \phi_A(H + \eta_2). \tag{C.10}$$

The linearized version of this equation is

$$\frac{1}{f}(\eta_2 - \eta_1) = \frac{1}{f_1}\eta_2 + \phi_A(H). \tag{C.11}$$

From (C.2) with $\phi_N = 0$ and (C.11), we obtain

$$\eta_1 = -\frac{\gamma_2 f \phi_A(H)}{\gamma_1(1 - f/f_1)^2 + \gamma_2}, \quad \eta_2 = \frac{\gamma_1 f(1 - f/f_1)\phi_A(H)}{\gamma_1(1 - f/f_1)^2 + \gamma_2}. \tag{C.12}$$

Because of the dependence of f on latitude, the amplitude of η_1 decreases southward, while that of η_2 slightly increases for $f/f_1 > (1 + \gamma_2/\gamma_1) - \sqrt{(\gamma_2/\gamma_1)(1 + \gamma_2/\gamma_1)}$. The potential thickness anomaly $(\eta_2 - \eta_1)/f$ is not conserved along the H contour but its magnitude is always larger than $|\phi_A|$, because the trajectory path is not along the H contour; the trajectory path shifts eastward when ϕ_A is positive and westward when ϕ_A is negative. Since H_2/f increases westward, the eastward shift of the trajectory path yields a positive potential thickness anomaly larger than ϕ_A.

N-mode crossing the internal boundary

The vertical structure of the stationary N-mode in the RY pool is different from that in the ventilated zone, so that the linear solution will be discontinuous at the internal boundary between them. This discontinuity must be canceled by the change in the location of the internal boundary. If the longitude of the internal boundary in the basic state is located at λ_B and the displacement caused by the N-mode is $\Delta\lambda$, the linearized potential thickness at $\lambda = \lambda_B + \Delta\lambda$ evaluated in the RY pool and in the ventilated zone can be written, respectively, as

$$\frac{1}{f}(\eta_2 - \eta_1)\Big|_{\lambda_{B-}} = \Delta Q_2, \tag{C.13}$$

$$\frac{1}{f}(\eta_2 - \eta_1)\Big|_{\lambda_{B+}} + \frac{1}{f}\frac{\partial H_2}{\partial \lambda}\Big|_{\lambda_{B+}} \Delta\lambda = \frac{\eta_2}{f_1}\Big|_{\lambda_{B+}} + \frac{1}{f_1}\frac{\partial H}{\partial \lambda}\Big|_{\lambda_{B+}} \Delta\lambda, \tag{C.14}$$

where the subscripts λ_{B-} and λ_{B+} denote the values at λ_B evaluated in the RY pool and in the ventilated zone, respectively, and ΔQ_2 is an anomaly of the homogenized potential thickness in the RY pool which occurs when the anomalous w_e forcing is applied at the outcrop latitude. The condition that they coincide to each other yields

$$\Delta\eta_2 - \Delta\eta_1 - \frac{\partial H_2}{\partial \lambda}\Big|_{\lambda_{B+}} \Delta\lambda = 0, \tag{C.15}$$

$$f_1 \Delta Q_2 - \eta_2|_{\lambda B+} - \frac{\partial H}{\partial \lambda}\Big|_{\lambda_{B+}} \Delta\lambda = 0, \tag{C.16}$$

where $\Delta\eta_j = \eta_j|_{\lambda_{B-}} - \eta_j|_{\lambda_{B+}}$. On the other hand, continuity of the Sverdrup function at $\lambda_B + \Delta\lambda$ requires

$$\gamma_1 H_1 \Delta\eta_1 + \gamma_2 H \Delta\eta_2 = 0. \tag{C.17}$$

Solving (C.15)–(C.17), we obtain the jumps in η_j at $\lambda = \lambda_B$ as

$$\Delta\eta_1 = \eta_1|_{\lambda_{B-}} - \eta_1|_{\lambda_{B+}} = \frac{\gamma_1 f H}{f_1 P_1}(f_1 \Delta Q_2 - \eta_2|_{\lambda_{B+}}), \tag{C.18}$$

$$\Delta\eta_2 = \eta_2|_{\lambda_{B-}} - \eta_2|_{\lambda_{B+}} = \frac{\gamma_1 f H_1}{f_1 P_1}(f_1 \Delta Q_2 - \eta_2|_{\lambda_{B+}}), \tag{C.19}$$

where we used (A.3). Since H is much larger than H_1, the jump in the upper interface is more significant than that in the lower interface.

REFERENCES

Chelton, D. B. and M. G. Schlax. 1996. Global observations of oceanic Rossby waves. Science, *272,* 234–238.

Craik, A. D. D. 1985. Wave Interactions and Fluid Flows, Cambridge University Press, 322 pp.

Deser, C., M. A. Alexander and M. S. Timlin. 1996. Upper-ocean thermal variations in the North Pacific during 1970–1991. J. Climate, *9,* 1840–1855.

de Szoeke, R. A. and D. B. Chelton. 1999. The modification of long planetary waves by homogeneous potential vorticity layers. J. Phys. Oceanogr., *29,* 500–511.

Dewar, W. R. and R. X. Huang. 2001. Adjustment of the ventilated thermocline. J. Phys. Oceanogr., *31,* 1676–1697.

Huang, R. X. and J. Pedlosky. 1999. Climate variability inferred from a layered model of the ventilated thermocline. J. Phys. Oceanogr., *29,* 779–790.

Killworth, P. D., D. B. Chelton and R. A. de Szoeke. 1997. The speed of observed and theoretical long extratropical planetary waves. J. Phys. Oceanogr., *27,* 1946–1966.

Liu, Z. 1999a. Planetary wave modes in the thermocline: non-Doppler-shift mode, advective mode and Green mode. Q. J. R. Meteorol. Soc., *125,* 1315–1339.

——— 1999b. Forced planetary wave response in a thermocline gyre. J. Phys. Oceanogr., *29,* 1036–1055.

Luyten, J. R., J. Pedlosky and H. Stommel. 1983. The ventilated thermocline. J. Phys. Oceanogr., *13,* 292–309.

Pedlosky, J. 1987. Geophysical Fluid Dynamics. 2nd ed. Springer-Verlag, 710 pp.

Polito, P. S. and P. Cornillon. 1997. Long baroclinic Rossby waves detected by TOPEX/POSEIDON. J. Geophys. Res., (C2)*102,* 3215–3235.

Rhines, P. B. and W. R. Young. 1982. A theory of the wind-driven circulation. I. Mid-ocean gyres. J. Mar. Res., *40*(Suppl.), 559–596.

Stephens, M., Z. Liu and H. Yang. 2001. Evolution of subduction planetary waves with application to North Pacific decadal thermocline variability. J. Phys. Oceanogr., *31,* 1733–1747.

Yasuda, T. and K. Hanawa. 1997. Decadal changes in the mode waters in the midlatitude North Pacific. J. Phys. Oceanogr., *27,* 858–870.

Young, W. R. and P. B. Rhines. 1982. A theory of the wind-driven circulation. II. Gyres with western boundary layers. J. Mar. Res., *40*(Suppl.), 849–872.

Received: *17 October, 2000;* revised: *22 January, 2002.*